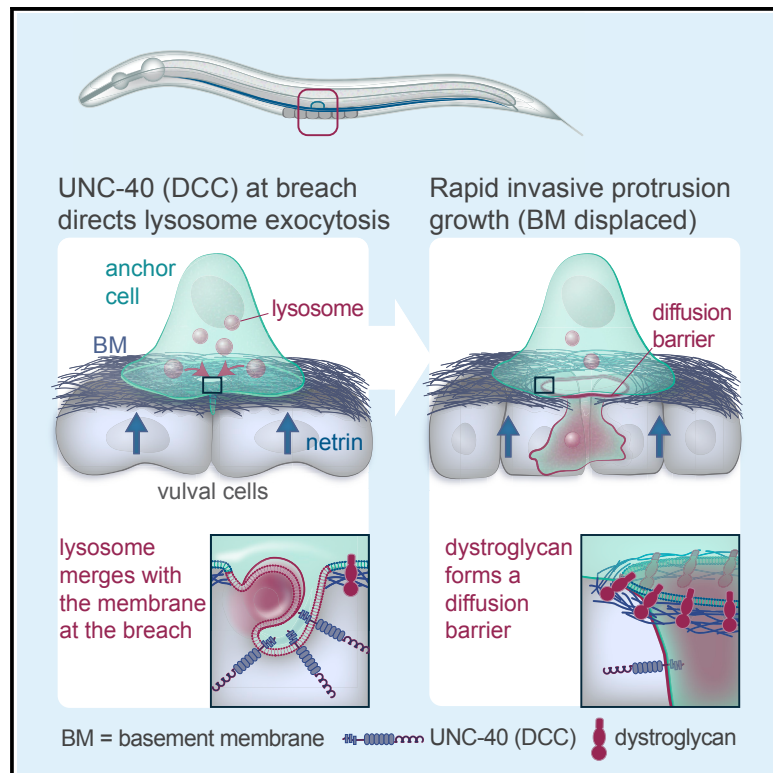


Developmental Cell

Cell Invasion *In Vivo* via Rapid Exocytosis of a Transient Lysosome-Derived Membrane Domain

Graphical Abstract



Authors

Kaleb M. Naegeli, Eric Hastie, Aastha Garde, ..., Qiuyi Chi, Bob Goldstein, David R. Sherwood

Correspondence

david.sherwood@duke.edu

In Brief

How do invasive cells clear an entry path after basement membrane breach? Naegeli et al. show in *Caenorhabditis elegans* that directed lysosome exocytosis regulated by a netrin-mediated pathway builds the large invasive protrusion formed after invadopodia. Isolated by a dystroglycan membrane diffusion barrier, the protrusion expands to create tissue openings.

Highlights

- Netrin receptor UNC-40 directs lysosome exocytosis to form an invasive protrusion
- UNC-40 mediates lysosome exocytosis through the t-SNARE SNAP-29 and the exocyst
- The membrane anchored MMP ZMP-1 localizes to the invasive protrusion
- A dystroglycan membrane diffusion barrier isolates the invasive protrusion



Cell Invasion *In Vivo* via Rapid Exocytosis of a Transient Lysosome-Derived Membrane Domain

Kaleb M. Naegeli,^{1,2} Eric Hastie,¹ Aastha Garde,¹ Zheng Wang,^{3,4} Daniel P. Keeley,¹ Kacy L. Gordon,¹ Ariel M. Pani,⁵ Laura C. Kelley,¹ Meghan A. Morrissey,^{6,7} Qiuyi Chi,¹ Bob Goldstein,⁵ and David R. Sherwood^{1,2,8,9,*}

¹Department of Biology, Regeneration Next, Duke University, 130 Science Drive, Box 90338, Durham, NC 27708, USA

²Department of Pharmacology and Cancer Biology, Duke University, Durham, NC 27708, USA

³Research Center for Tissue Engineering and Regenerative Medicine, Union Hospital, Tongji Medical College, Huazhong University of Science and Technology, Wuhan, Hubei 430022, China

⁴Department of Gastrointestinal Surgery, Union Hospital, Tongji Medical College, Huazhong University of Science and Technology, Wuhan, Hubei 430022, China

⁵Biology Department and Lineberger Comprehensive Cancer Center, University of North Carolina at Chapel Hill, Chapel Hill, NC 27599, USA

⁶The Howard Hughes Medical Institute, University of California, San Francisco, San Francisco, CA 94158, USA

⁷Department of Cellular and Molecular Pharmacology, University of California, San Francisco, San Francisco, CA 94158, USA

⁸Regeneration Next, Duke University, Durham, NC 27710, USA

⁹Lead Contact

*Correspondence: david.sherwood@duke.edu

<https://doi.org/10.1016/j.devcel.2017.10.024>

SUMMARY

Invasive cells use small invadopodia to breach basement membrane (BM), a dense matrix that encases tissues. Following the breach, a large protrusion forms to clear a path for tissue entry by poorly understood mechanisms. Using RNAi screening for defects in *Caenorhabditis elegans* anchor cell (AC) invasion, we found that UNC-6(netrin)/UNC-40(DCC) signaling at the BM breach site directs exocytosis of lysosomes using the exocyst and SNARE SNAP-29 to form a large protrusion that invades vulval tissue. Live-cell imaging revealed that the protrusion is enriched in the matrix metalloprotease ZMP-1 and transiently expands AC volume by more than 20%, displacing surrounding BM and vulval epithelium. Photobleaching and genetic perturbations showed that the BM receptor dystroglycan forms a membrane diffusion barrier at the neck of the protrusion, which enables protrusion growth. Together these studies define a netrin-dependent pathway that builds an invasive protrusion, an isolated lysosome-derived membrane structure specialized to breach tissue barriers.

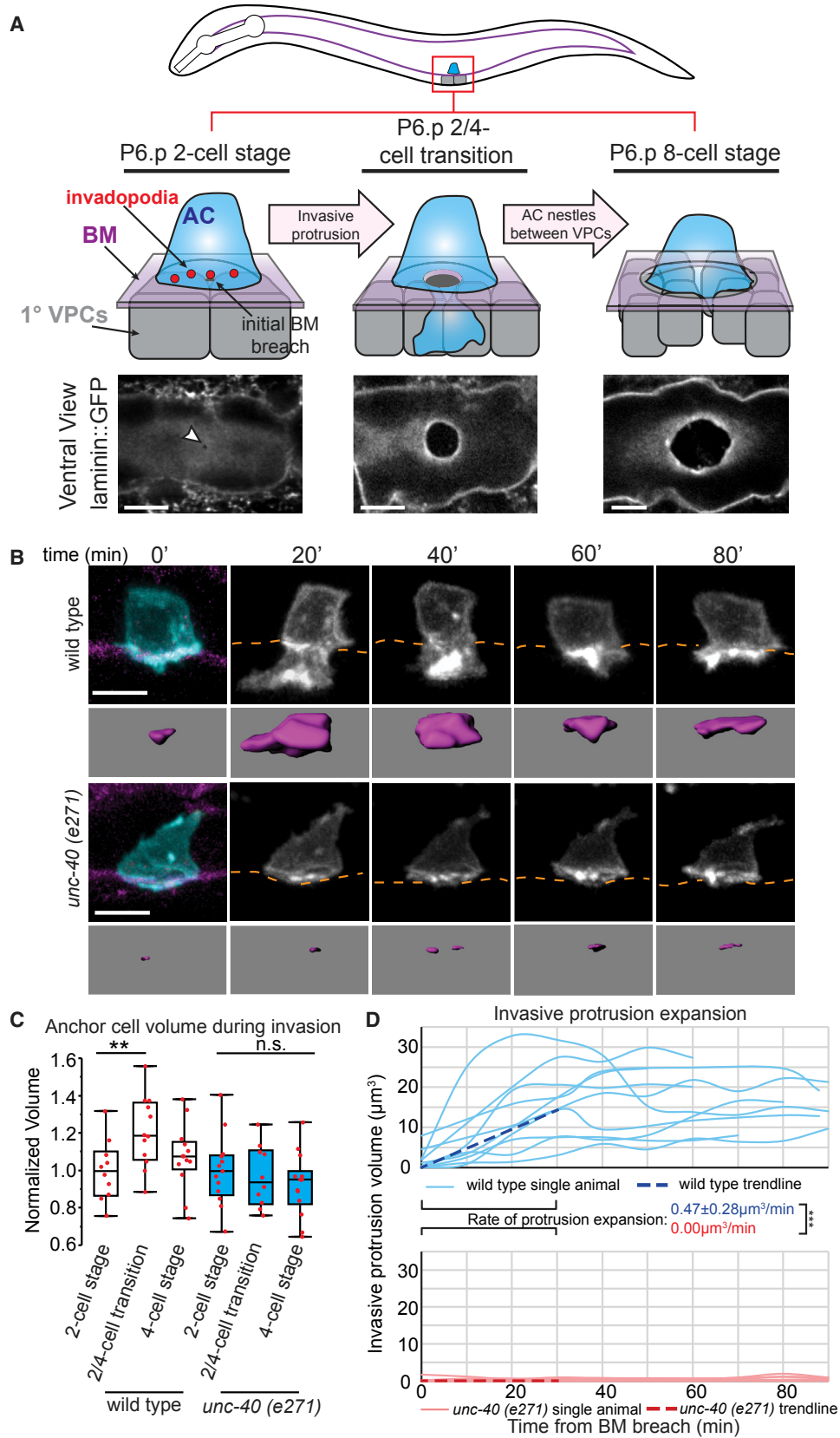
INTRODUCTION

The ability of cells to invade and enter tissues is crucial for many developmental and physiological processes, including trophoblast implantation, neural crest migration, and leukocyte trafficking (Lohmer et al., 2014; Madsen and Sahai, 2010). Misregulation of invasion also underlies numerous inflammatory diseases, developmental disorders, and metastasis (Hagedorn

and Sherwood, 2011). The first barrier an invading cell encounters is usually a basement membrane (BM), a dense, highly cross-linked extracellular matrix that supports and surrounds tissues (Yurchenco, 2011). Invasive cells use small, matrix metalloprotease (MMP)-rich membrane-associated F-actin structures called invadopodia to create small breaches in BM (Lohmer et al., 2014; Murphy and Courtneidge, 2011). Mechanisms regulating invadopodia formation and turnover have been extensively examined using 2D *in vitro* assays that mimic flat BM surfaces (Beaty and Condeelis, 2014). The events that follow invadopodium penetration of BM, however, are less clear, as this step in invasion is challenging to visualize in complex vertebrate tissues, and this stage is difficult to recapitulate with *in vitro* and *ex vivo* invasion assays (Beerling et al., 2011; Friedl and Wolf, 2010).

The *Caenorhabditis elegans* anchor cell (AC) carries out a highly stereotyped cell invasion event that is experimentally accessible to live-cell imaging and genetic perturbations (Sherwood and Sternberg, 2003). The AC uses dynamic, rapidly forming and disassembling invadopodia to breach the BM separating the uterine tissue from the vulval tissue (Hagedorn et al., 2013, 2014; Lohmer et al., 2016). Approximately ten invadopodia are found at any one time prior to invasion. At the site of the initial invadopodium-mediated BM breach, the netrin receptor UNC-40 (the *C. elegans* ortholog of vertebrate DCC) becomes enriched, and in response to secreted UNC-6 (netrin) directs the formation of a single large invasive protrusion (Hagedorn et al., 2013). This invasive protrusion shuts down further invadopodia production, and dramatically widens the BM opening by degrading and physically displacing the BM as it extends between and contacts the central vulval cells, thus securing uterine-vulval connection (Figure 1A). A few *ex vivo* invasion studies and tumor tissue sections have also noted the transition of invadopodia to a single large protrusion, as well as the presence of large protrusions that cross BMs in cancer cells (Hotary et al., 2006; Leong et al., 2014; Schoumacher et al., 2010), suggesting that this later, poorly understood aspect of the invasion program is conserved.





(legend on next page)

BMs and tissues are rigid and densely packed (Halfter et al., 2015), and it is unclear if invasive cells alter their shape, add membrane from internal pools, or harbor membrane within plasma membrane folds to extend large protrusions within the tight confines of tissues to open a path for the invading cell. Interestingly, during invadopodia formation, the membrane-tethered MMP (MT1-MMP) is dynamically recycled through endosomes and lysosomes to deliver MT1-MMP to invadopodia at the cell surface (Castro-Castro et al., 2016). Whether the invasive protrusion can harness the same membrane compartments to form the large invasive protrusion or uses another membrane source for this distinct invasive structure is not known.

Using quantitative live-cell imaging, genetic analysis, and misexpression studies, we examined the formation of the AC invasive protrusion. We found that UNC-6/UNC-40 interactions localize lysosomes to the site of protrusion formation and that LMP-1 (a lysosomal protein) and ZMP-1 (a membrane-tethered MMP localized to lysosomes) are enriched in the invasive protrusion. The invasive protrusion locally increases the size of the AC by more than 20%, which may contribute strong pushing forces to open a gap in the BM and vulval tissue. Through lysosome perturbation and a focused RNAi screen, we found that lysosome integrity and the exocytic machinery are required for invasive protrusion growth, suggesting that lysosomes are exocytosed to form the protrusion. In addition, photobleaching of the invasive protrusion membrane and genetic perturbation studies revealed that it is isolated from the AC body by a diffusion barrier formed by the BM adhesion receptor dystroglycan, and that this barrier promotes protrusion growth. Together, these results reveal a netrin-mediated pathway directs the formation of the invasive protrusion: a distinct lysosome-derived membrane domain that is rapidly exocytosed to breach tissue barriers.

RESULTS

The Invasive Protrusion Forms from Localized Plasma Membrane Expansion

Previous studies by our group found that small, rapidly forming (~1 minute lifetime) invadopodia breach the BM during AC invasion into the vulval epithelium in *C. elegans*. Following BM penetration, invadopodia formation ceases, and a large, longer-lived protrusion extends at the site of breach in an UNC-40 (netrin receptor)-dependent manner (Hagedorn et al., 2013). UNC-40

is not required for invadopodia formation, indicating that invadopodia and the invasive protrusion are regulated distinctly (Morrisey et al., 2013). We hypothesized two possible mechanisms for expansion of the protrusion: redistribution of the plasma membrane, which would not yield an increase in AC size, or addition of new membrane, which would increase the size of the AC. To begin to distinguish between these two possibilities, we first quantified plasma membrane dynamics during AC invasion using AC-specific expression of GFP tagged with a CAAX prenylation motif (*cdh-3*>GFP::CAAX), which localizes to plasma membranes. We measured the surface area and volume of the AC throughout the approximately 1.5-hr invasion process (see STAR Methods). The timing of invasive protrusion maturation was assessed using the underlying P6.p vulval precursor cell (VPC) divisions, which adopt a 1° vulval fate and divide in synchrony with AC invasion (Figure 1A). During formation of the invasive protrusion (P6.p 2/4-cell transition), the AC increased 12.7% in surface area and 20.6% in volume (Figures 1B, 1C, and S1A). Protrusion growth occurred during an average 55-min window (Figure S1B; n = 23 animals), with maximum protrusion growth and the fastest invasive protrusions reaching maximal size at 30 min (average growth rate of 0.47 $\mu\text{m}^3/\text{min}$ for 30 min following BM breach, n = 10 animals; Figures 1B and 1D; Movie S1). AC growth was specifically localized to the single invasive protrusion (Figure S1C). While invadopodia first breach the BM and make a small hole, invasive protrusion expansion was correlated with enlargement of the BM hole (as visualized with the major BM component laminin::GFP; Figures 1A and S1D), supporting the idea that the protrusion actively clears a large BM opening during vulval tissue invasion. Following growth, the invasive protrusion retracted (early P6.p 4-cell stage; n = 10 animals observed; Figure 1B; Movie S1), and the AC volume and surface area returned to their approximate original sizes (Figures 1C and S1A). Similar protrusion dynamics were observed in three strains expressing two membrane markers (see the STAR Methods), indicating invasive protrusion formation is robust and stereotyped. Notably, ACs from animals lacking the netrin receptor UNC-40 (vertebrate DCC), which is required to form the invasive protrusion (Hagedorn et al., 2013), did not increase in volume or surface area (average growth rate of 0.00 $\mu\text{m}^3/\text{min}$; for this and all other experiments, growth rates were calculated during the first 30 min of protrusion growth after BM breach; Figures 1B–1D and S1A;

Figure 1. The Invasive Protrusion Locally Increases AC Area and Volume

(A) AC invasion in *C. elegans* (top, lateral view schematic; bottom, ventral view of laminin::GFP-labeled BM). Left: during the early L3 larval stage, the AC (blue) sits atop the BM (purple) and the two P6.p VPC descendants (1° VPCs, gray). Actin-rich invadopodia (red) form, and one breaches, the BM (arrow top, arrowhead bottom). Center: the time the underlying P6.p descendants divide, the invasive protrusion expands, and the BM hole widens. Right: by completion of next P6.p descendant division, the BM opening has expanded beyond the border of the AC, the invasive protrusion has retracted, and the AC contacts the central P6.p descendants.

(B) Time-lapse image of AC invasive protrusion formation. AC membrane labeled by *cdh-3*>GFP::CAAX, blue and grayscale; BM (laminin::mCherry, magenta) position shown by orange dotted lines. Wild-type (top) and *unc-40* (*e271*) (bottom) animals. Invasive protrusion isosurfaces (the portion of the AC below the BM, purple).

(C) AC volume before protrusion formation (P6.p 2-cell stage), during protrusion expansion (P6.p 2/4-cell transition), and after retraction (P6.p 4-cell stage) for wild-type (white) and *unc-40* (*e271*) mutants (blue). Volume is normalized to AC volume of corresponding genotype before invasion (see the STAR Methods; n > 10 each category; **p < 0.01, n.s., not significant [p > 0.05], one-way ANOVA with Tukey HSD *post-hoc* test).

(D) AC protrusion volume over time in wild-type (blue) and *unc-40* (*e271*) (red) animals from the time of BM breach until time lapse ended (time points shown every 10 min; see the STAR Methods). In this and all subsequent figures, protrusion volume growth was compared over the first 30 min of protrusion growth, the time of maximum growth in wild-type animals. Average expansion rates (dotted lines) \pm SD are shown (n = 10 animals for each group; ***p < 0.001 n.s., not significant [p > 0.05], Student's t test).

Scale bars, 5 μm . See also Figure S1.

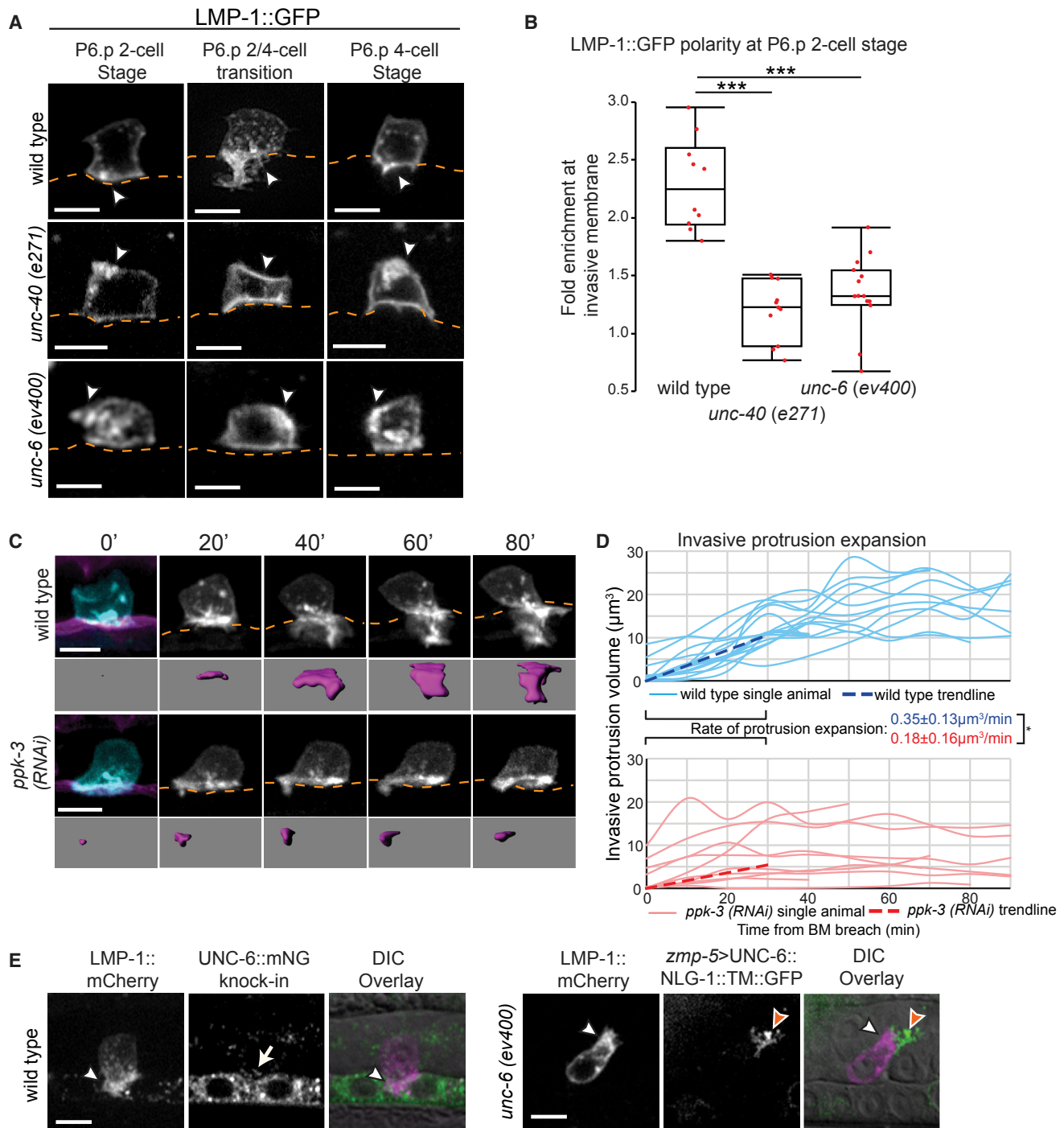


Figure 2. UNC-6 (netrin) Polarizes Lysosomes to Build the Invasive Protrusion

(A) Lysosomes (LMP-1::GFP) in the ACs of wild-type (top), *unc-40 (e271)* (middle), and *unc-6 (ev400)* (bottom) animals before protrusion formation (P6.p 2-cell stage), during protrusion expansion (P6.p 2/4-cell transition), and after retraction (P6.p 4-cell stage). Arrowheads indicate lysosome localization. BM position, orange.

(B) Polarity of LMP-1::GFP at the AC invasive membrane before BM breach ($n \geq 11$ animals per genotype; *** $p < 0.001$, one-way ANOVA with Tukey HSD *post-hoc* test).

(C) Time-lapse images of AC invasive protrusion formation in a uterine-specific RNAi background. AC membrane labeled with *cdh-3>mCherry::PLCδ^{PH}*, blue and grayscale, purple isosurface below; BM (laminin::GFP, magenta) position shown by orange dotted lines.

(D) AC protrusion volume over time in control (blue) and *ppk-3 (RNAi)* (red) animals. Average expansion rates (dotted lines) \pm SD for the first 30 min of protrusion growth ($n = 14$ animals for wild-type, $n = 10$ animals for *ppk-3 (RNAi)*; * $p < 0.05$, Student's *t* test).

(legend continued on next page)

Movie S1). Together, these results indicate that UNC-40 directs the formation of a large protrusion that locally expands the size of the AC to open a single large gap in the BM. This is in marked contrast to the distinctly different action of invadopodia, which breach BM, are more numerous, smaller, short lived, and not directed by UNC-40 (Hagedorn et al., 2013, 2014; Lohmer et al., 2016).

Lysosomes Contribute Membrane to Form the Invasive Protrusion

Lipid membranes can only stretch their surface area by 2%–3% before rupturing (Mohandas and Evans, 1994). To dynamically increase surface area, cells add membrane from membrane folds or through exocytosis of internal membrane stores (Kay et al., 2008). Previous staining with the outer-membrane dye, FM1-43, suggested that the AC plasma membrane lacks membrane folds (Hagedorn et al., 2013), and we ruled out folds as the source of protrusion membrane by transmission electron microscopy (Figure S2A). A number of internal membrane sources provide lipids for plasma membrane expansion, including the endoplasmic reticulum (ER), the Golgi apparatus, endosomes, and lysosomes (Dyer et al., 2007; Lecuit and Pilot, 2003; Lecuit and Wieschaus, 2000; Raiborg et al., 2015; Rodriguez et al., 1997). We examined worms expressing fusion proteins that mark the ER (CYTB-5.1::GFP), the Golgi apparatus (AMAN-2::GFP), early endosomes (mCherry::RAB-5), late endosomes (mCherry::RAB-7), recycling endosomes (mCherry::RAB-11), and lysosomes (LMP-1::GFP and GFP::CUP-5) (Sato et al., 2014). We hypothesized that if one of these membrane sources builds the protrusion, it should localize to the BM breach site. Notably, LMP-1::GFP- and CUP-5::GFP-positive vesicles were polarized strongly along the AC's invasive membrane prior to invasive protrusion formation (Figures 2A, S2B, and S2C). Further, both lysosome markers were enriched within the invasive protrusion during its growth ($n = 20/20$ animals; Figures 2A and S2D).

Lysosomes are known to play roles in invasion via secretion or delivery of membrane-associated proteases (Castro-Castro et al., 2016; Kirkegaard and Jäättelä, 2009), but they have never been investigated as potential membrane sources for building invasive structures in cells. To test if the invasive protrusion is formed from lysosomal membrane, we used RNAi knockdown of the phosphatidylinositol phosphate kinase *ppk-3*, which regulates the maturation and integrity of lysosomes (Nicot et al., 2006). Because the null allele of *ppk-3* is lethal (Nicot et al., 2006), we performed these experiments using a uterine-specific RNAi strain (see the STAR Methods). Importantly, knockdown of *ppk-3* decreased the total amount of LMP-1-positive vesicles within the AC, but not early endosomes (RAB-5 marked) or late endosomes (RAB-7 marked) (Figure S2E), indicating a specific loss of lysosomes in the AC. Knockdown of *ppk-3* in the uterine cells strongly perturbed AC invasion (Table S1) and invasive protrusion formation (Figure 2C). As other uterine cells do not

contribute to AC invasion (Sherwood and Sternberg, 2003), these data indicate that *ppk-3* function is specifically required in the AC for invasion. Quantification of invasive protrusion growth revealed that loss of *ppk-3* resulted in a significantly reduced rate of invasive protrusion growth (0.18 versus $0.35 \mu\text{m}^3/\text{min}$ in control animals; Figures 2C and 2D; Movie S2), and the volume of the AC did not increase (Figure S2F), consistent with an absence of membrane addition. Taken together, these observations suggest that lysosomes contribute membrane to form the invasive protrusion.

Netrin/DCC Interactions Direct Lysosome Polarity

The netrin receptor UNC-40 (vertebrate DCC) localizes to the site of BM breach and organizes invasive protrusion formation in response to UNC-6 (netrin). If lysosomes are a local membrane source for the protrusion, we hypothesized that the UNC-6/UNC-40 interaction may polarize them. Consistent with this notion, LMP-1-labeled lysosomes were no longer polarized at the invasive membrane prior to or during the normal time of invasion in *unc-40* (*e271*) and *unc-6* (*ev400*) mutants (Figures 2A and 2B; polarity was calculated as enrichment of lysosomes at the invasive cell membrane compared with density at the apical membrane; see the STAR Methods).

To examine how endogenous UNC-6 acts to polarize lysosomes to form the protrusion, we used CRISPR/Cas9 to fuse the coding sequence of fluorescent protein mNeonGreen (mNG) to the *unc-6* genomic locus (*unc-6::mNG* knockin) (Shaner et al., 2013). UNC-6::mNG was detected at high levels in the P6.p VPC and its descendants prior to and during protrusion formation, as well as in extracellular punctae around the AC and its invasive protrusion ($n = 12/12$ animals, Figure 2E). These results suggest that a short-range UNC-6 signal is present on the ventral side of the AC to polarize lysosomes to the site of protrusion formation.

To directly test whether UNC-6 is sufficient to polarize lysosomes, we expressed a membrane-tethered form of UNC-6 in the dorsal uterine cells (*zmp-5>UNC-6::NLG-1::TM::GFP*) in *unc-6* (*ev400*) null animals (Figure 2E) (Wang et al., 2014). In *unc-6* null mutants alone, lysosomes are mispolarized (Figure 2A), no protrusion forms, and AC invasion fails (Ziel et al., 2009). Dorsal presentation of UNC-6, however, robustly directed lysosomes (marked with LMP-1::GFP) toward ectopic UNC-6 ($n = 15/15$ animals) and in some cases the AC extended a small LMP-1-enriched protrusion toward the ectopic UNC-6 ($n = 6/15$ animals; Figure 2E). These observations suggest that localized UNC-6 directs the polarized addition of lysosomal membrane to form the invasive protrusion.

The t-SNARE SNAP-29 Promotes Invasive Protrusion Formation

Localized exocytosis of the lysosomes that concentrate at the breach site might add membrane to promote invasive protrusion formation. To test this idea, we performed an RNAi screen of 116

(E) Lysosomes (LMP-1::mCherry, magenta) polarize within the invasive protrusion (arrowhead) toward UNC-6::mNG (green, *unc-6* (*cp190*)), which is expressed in the VPCs and localizes in extracellular punctae (arrow). An *unc-6* (*ev400*) mutant with membrane-tethered UNC-6 (*zmp-5>unc-6::nlg-1::TM::GFP*) expressed in a dorsal uterine cell (orange arrowhead). The AC extends a small protrusion with the lysosome marker LMP-1::mCherry (white arrowhead) polarized toward the ectopic UNC-6::GFP.

Scale bars, 5 μm . See also Figure S2.

genes encoding proteins involved in membrane trafficking, looking for perturbations in AC invasion (Sato et al., 2014). RNAi-mediated knockdown of 22 genes yielded defects in AC invasion (Table S2). In addition, loss of the *C. elegans* vertebrate Rab11 orthologs *rab-11.1* and *rab-11.2*, which primarily regulate recycling endosomes (Grant and Donaldson, 2009; Stenmark, 2009), disrupted invasive protrusion retraction (Figure S3A). Both whole-body and uterine-specific targeting of *rab-11.1* and *rab-11.2* disrupted retraction at the P6.p 4-to-6-cell stage transition (in 6/10 and 17/62 whole-body RNAi-treated animals, and in 8/22 and 2/15 uterine-specific RNAi-treated animals the ACs' invasive protrusion was not retracted, respectively, versus 1/22 ACs in wild-type animals), suggesting that membrane recycling is important for protrusion withdrawal. As depletion of the SNAP-25-family t-SNARE *snap-29* produced the strongest defect in invasion (Table S2), we characterized the function of SNAP-29 during protrusion formation.

The vertebrate ortholog of *snap-29* (SNAP25) promotes exocytosis and plasma membrane expansion during axon branch formation through interactions with the vertebrate *unc-40* ortholog DCC (Winkle et al., 2014), and thus might form a conserved polarized membrane addition circuit. Supporting this possibility, UNC-40 contains the intracellular P3 domain that has been implicated in regulating interactions with vertebrate SNAP25 during exocytosis (Winkle et al., 2014; Ziel and Sherwood, 2010). Uterine-specific RNAi knockdown of *snap-29* disrupted AC invasion to the same extent as whole-body treatment (Table S1), suggesting that SNAP-29 functions in the AC. A *snap-29*>GFP transcriptional reporter was expressed in the AC and mCherry::SNAP-29 was polarized to the invasive membrane before invasion and concentrated in the invasive protrusion (Figures 3A and S3B). The lysosome marker LMP-1::GFP and mCherry::SNAP-29 co-localized at the invasive surface of the AC and in the invasive protrusion (Figures 3B and 3C), suggesting that SNAP-29 may mediate lysosome exocytosis to form the invasive protrusion. Consistent with this idea, uterine-specific knockdown of *snap-29* resulted in a reduction of invasive protrusion growth rate and protrusion volume (Figures 3D and 3E; Movie S3), and AC size did not increase (Figure S3C). Loss of *unc-40* did not alter SNAP-29 polarity, indicating that SNAP-29 is enriched at the invasive membrane independent of UNC-40 (Figure S3D). Importantly, knockdown of *snap-29* also did not affect UNC-40 polarization at the invasive membrane (Figures S3E and S3F) or lysosome polarization (Figure S3G), indicating that *snap-29* does not alter the invasive protrusion through misregulation of UNC-40 or lysosome localization. Taken together, these data suggest that SNAP-29 directs exocytosis of lysosomes to form the invasive protrusion.

The Exocyst Complex Is Required for Generating the Invasive Protrusion

Three components of the exocyst complex were also identified in our screen (Table S2). The exocyst complex regulates transport, tethering, and docking of vesicles prior to SNARE function at the plasma membrane (He and Guo, 2009), and is composed of eight subunits, encoded in *C. elegans* by the genes *sec-3*, *sec-5*, *sec-6*, *sec-8*, *sec-10*, *sec-15*, *exoc-7*, and *exoc-8* (Jiu et al., 2012). Uterine-specific RNAi knockdown of exocyst components yielded defects in AC invasion (Table S1), suggesting

that the complex acts in the AC. Endogenously tagged SEC-5::YFP was expressed in the AC, but it and other exocyst components were not polarized (Figure S4A) (Armenti et al., 2014). We assayed protrusion formation in a null mutant of *exoc-8* (*ok2523*), which is a regulatory subunit not required for animal viability (Jiu et al., 2012). ACs in *exoc-8* mutants breached the BM, but had dramatically diminished rates of protrusion growth and volume (Figures 4A and 4B; Movie S4). Consistent with a lack of exocytosis, the ACs in *exoc-8* mutants also did not increase in size (Figure S4B). Notably, UNC-40::GFP and LMP-1::mCherry polarities were normal in *exoc-8* (*ok2523*) mutants (Figures S4C and S4D), indicating that the exocyst complex is not necessary for UNC-40 or lysosome localization. Together, these data provide evidence that invasive protrusion formation requires exocytosis of lysosomes, which is mediated by the exocyst complex and the SNAP-25 family t-SNARE SNAP-29.

The Invasive Protrusion Is an Isolated Membrane Domain

We noted that LMP-1::GFP, a transmembrane protein and marker of lysosomes, was concentrated along the cell surface of the invasive protrusion (Figure 2A). This localization raised the possibility that the invasive protrusion membrane is isolated from the rest of the AC and may be a specialized invasive structure. To further test this idea, we examined the localization of the GPI-anchored membrane-associated MMP ZMP-1, which promotes BM removal during AC invasion (Sherwood et al., 2005). A ZMP-1 localization reporter (*zmp-1*>GFP::*zmp-1-GPI*) co-localized with the lysosome marker LMP-1 prior to AC invasion (Figures S5A and S5B; n = 5 animals), and was strongly enriched in the invasive protrusion (Figures 5A and 5B; n = 22/22 animals). These observations support the idea that the invasive protrusion is a specialized structure and that it might be a distinct membrane domain.

If the invasive protrusion is a distinct membrane domain, fluorescence loss in photobleaching (FLIP) would show that photobleached GFP::CAAX from the AC cell body does not diffuse into the protrusion (and *vice versa*). We performed FLIP in ACs prior to protrusion formation (P6.p 2-cell stage), during protrusion formation (P6.p 2/4-cell transition) and after retraction (P6.p 8-cell stage), by photobleaching a 1- μ m diameter region of the AC membrane and measuring the rate of GFP loss. When targeting the body of the AC, we observed a significantly higher rate of GFP signal loss in the body than in the protrusion (Figures 5C and 5D). Reciprocal FLIP of the protrusion revealed a similar rate of GFP signal loss localized to the protrusion (Figures 5C and 5D). In contrast, in ACs that had not yet formed a protrusion and in ACs after protrusion retraction, we found close rates of GFP signal loss throughout the AC (Figures 5C and 5D). We conclude that the invasive protrusion membrane harbors unique proteins and is a separate compartment that is isolated from the rest of the AC.

An Expanding Ring of Dystroglycan and F-Actin Localizes to the Neck of the Protrusion

Our FLIP results suggested that a membrane diffusion barrier may separate the invasive protrusion from the AC body. Membrane diffusion barriers impede lipid and protein movement in structures such as tight junctions in epithelial cells and the

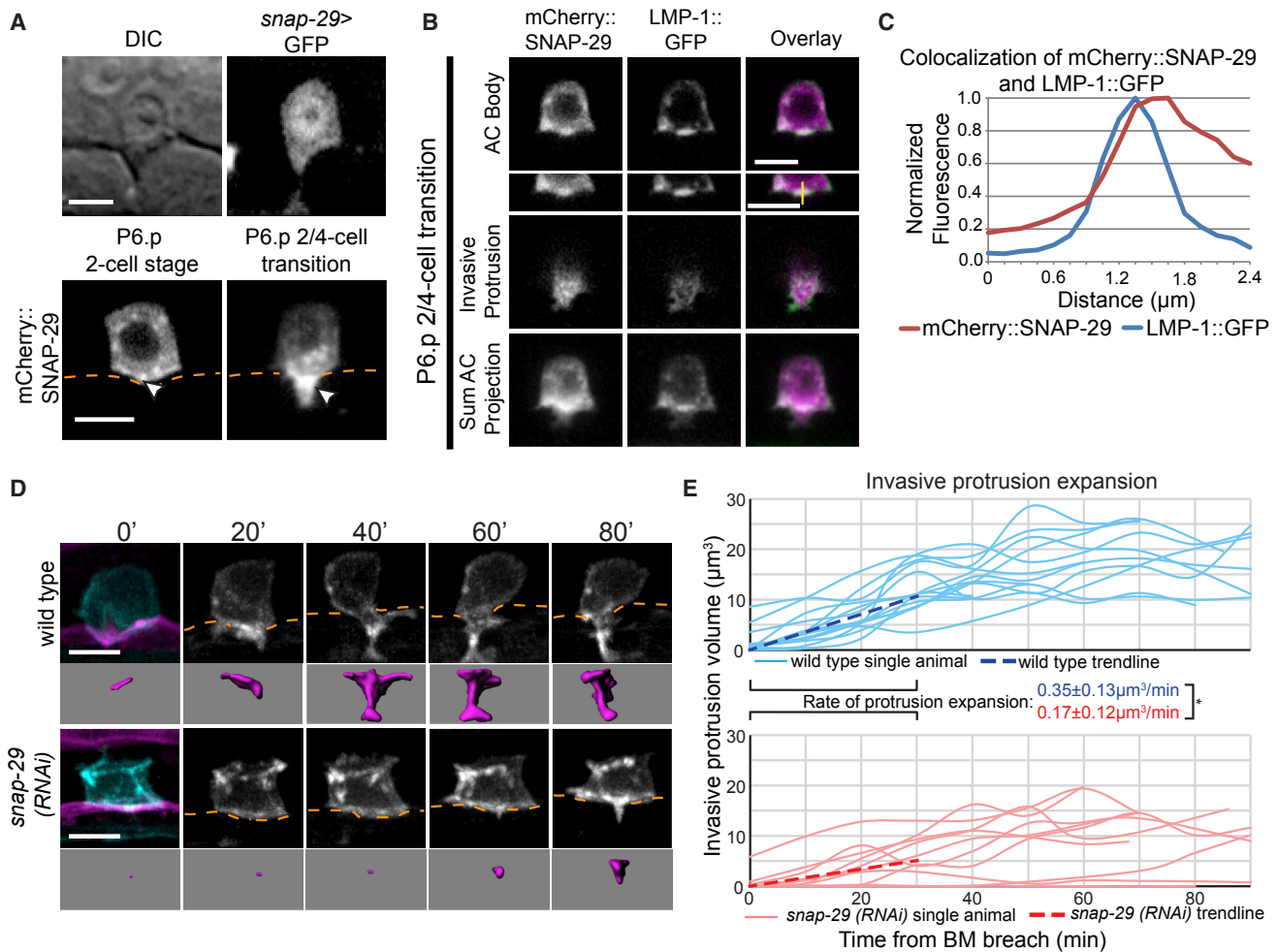


Figure 3. The t-SNARE SNAP-29 Facilitates Invasive Protrusion Expansion

(A) A *snap-29* transcriptional reporter (*snap-29>GFP*; top right) expressed in the AC. An AC-expressed translational reporter (*cdh-3>mCherry::SNAP-29*; bottom) is polarized (arrowheads) to the invasive membrane before invasion (left) and within the protrusion (right); BM position, orange.

(B) Colocalization of mCherry::SNAP-29 and LMP-1::GFP during protrusion formation: 0.5- μm confocal z slices of the AC body (top) and invasive protrusion (middle); sum projection of the AC (bottom). Yellow line (top inset, right) indicates point of fluorescence measurement shown in (C).

(C) Fluorescence measurement shows colocalization of peak SNAP-29 (red) and LMP-1 (blue) signal.

(D) Time-lapse images of AC protrusion formation in a uterine-specific RNAi strain. AC membrane labeled by *cdh-3>mCherry::PLC3^{PH}*, blue and grayscale, purple isosurface below; BM (laminin::GFP, magenta) position shown by orange dotted lines.

(E) AC protrusion volume over time for wild-type (blue) and *snap-29 (RNAi)* (red) animals. Average expansion rates (dotted lines) \pm SD for first 30 min of protrusion growth ($n = 14$ animals for control, $n = 10$ animals for *snap-29 (RNAi)*); * $p < 0.05$, Student's t test). Wild-type controls were the same as in Figure 2D.

Scale bars, 5 μm . See also Figure S3.

axon hillock in neurons, where cytoskeletal and transmembrane proteins are concentrated (Trimble and Grinstein, 2015). Because the neck of the invasive protrusion, which contacts the BM, appeared to be the boundary between the invasive protrusion and AC body (Figure 5C), we hypothesized that a BM adhesion receptor might concentrate at the neck of the protrusion and form a diffusion barrier.

The two major classes of adhesion receptors that link BM to the cytoskeleton are integrin family members and the receptor dystroglycan (Bello et al., 2015; Yurchenco, 2011). The INA-1/PAT-3 heterodimer is the only integrin expressed in the AC at the time of invasion (Hagedorn et al., 2009), where it is required for invadopodia formation (Hagedorn et al., 2013). A functional

PAT-3::GFP fusion protein, however, was not concentrated at the neck of the invasive protrusion (Figure S6A; $n = 19/19$ animals). To examine dystroglycan localization, we used CRISPR/Cas9 to fuse the coding sequence of mNG to the *dgn-1* genomic locus (*dgn-1::mNG* knockin). DGN-1::mNG was present at high levels in the AC prior to and throughout invasion. Importantly, DGN-1::mNG was enriched at the AC-BM interface in an expanding ring at the neck of the invasive protrusion during its growth (Figure 6A; $n = 26/27$ animals). Following retraction, when the AC loses contact with the BM and moves between the central vulval cells, DGN-1::mNG enrichment on the basal sides of the AC was lost (Figure 6A; $n = 15/15$ animals). As actin networks also contribute to diffusion barriers (Trimble and

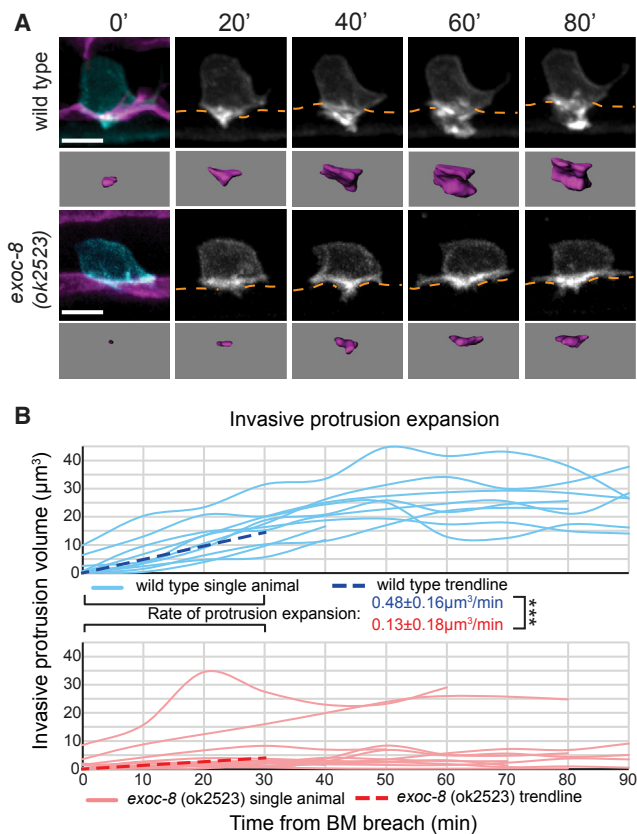


Figure 4. The Exocyst Complex Promotes Invasive Protrusion Formation

(A) Time-lapse images of AC protrusion formation. AC membrane labeled by *cdh-3>mCherry::PLC δ^{PH}* , blue and grayscale, purple isosurface below; BM (laminin::GFP, magenta) position shown by orange dotted lines.

(B) AC protrusion volume over time for wild-type (blue) and *exoc-8 (ok2523)* (red). Average expansion rates (dotted lines) \pm SD for first 30 min of protrusion growth ($n = 10$ animals for wild-type, $n = 13$ animals for *exoc-8 (ok2523)*; *** $p < 0.001$, Student's *t* test). Asterisks indicate statistical significance, see STAR Methods.

Scale bars, 5 μm . See also Figure S4.

Grinstein, 2015), we next examined the localization of F-actin. Notably, a similar localization pattern at the neck of the protrusion was observed for F-actin (Figures 6B and 6C; $n = 24/24$ and $15/15$ animals, respectively). These observations indicate that dystroglycan and F-actin form a ring at the neck of the invasive protrusion, which may function as a membrane diffusion barrier that isolates the protrusion from the AC body.

Dystroglycan Acts as a Diffusion Barrier and Promotes Protrusion Growth

To test whether dystroglycan functions as a diffusion barrier, we performed time-lapse analysis of invasive protrusion formation following uterine-specific RNAi knockdown of *dgn-1*. Knockdown of *dgn-1* (an average 75% reduction of DGN-1::mNG fluorescence within the AC; Figure S6B) resulted in a dramatic reduction in invasive growth rate and volume (Figures 6D and 6E; Movie S5), and the overall size of the AC failed to increase (Figure S6C). We performed FLIP analyses on ten animals after

dgn-1 knockdown, and these animals showed an increased rate of GFP diffusion between the small invasive protrusions and the AC body compared with controls (Figures 6F and 6G), indicating a breakdown of the diffusion barrier. We also examined ZMP-1 reporter localization after dystroglycan knockdown. The ZMP-1 reporter was still enriched in the reduced protrusions (Figures S6D and S6E). However, as the ZMP-1 reporter localizes to lysosomes, which are polarized by UNC-6/UNC-40 interactions at the invasive membrane (Figures 2A and 2B), it is possible that UNC-40 is sufficient to concentrate ZMP-1 within the reduced protrusions. RNAi knockdown of *dgn-1* did not significantly impact the localization of F-actin to the AC-BM interface at the necks of the smaller invasive protrusions (Figure S6F), suggesting that a DGN-1-independent mechanism regulates actin localization. Notably, loss of INA-1/PAT-3 (integrin), either through a viable loss-of-function *ina-1* allele (*gm39*) or a dominant-negative form of *pat-3* expressed in the AC (Hagedorn et al., 2009), did not alter invasive protrusion formation or disrupt the membrane diffusion barrier (Figures S6G–S6I). Thus, integrin is neither localized to, nor functionally involved in, the AC protrusion diffusion barrier. These observations suggest that a diffusion barrier set up by dystroglycan-BM interactions at the neck of the AC promotes invasive protrusion growth by maintaining it as a distinct membrane domain.

We further tested whether BM contact with the neck of the invasive protrusion is necessary for the polarized addition of a large amount of membrane. The invasive protrusions that formed in response to ectopic UNC-6 (Figure 2E) do not breach or otherwise interact with a BM. As they rarely formed protrusions, we wanted to more carefully examine protrusions by using a marker for F-actin (*cdh-3>moeABD::mCherry*) in the AC. Consistent with the requirement for a BM-dependent diffusion barrier, most ACs failed to form a protrusion upon contacting ectopic UNC-6 ($n = 18/26$ ACs observed). The few protrusions that did form were much smaller than normal invasive protrusions (Figures 7A and 7B). Taken together, our observations indicate that the AC invades into the vulval tissue by forming a membrane diffusion barrier at the AC-BM interface, which allows localized exocytosis of lysosomes to promote expansion of a large, MMP-enriched protrusion that breaches tissue boundaries.

DISCUSSION

The importance of invadopodia in breaching BM and the mechanisms regulating their formation are well established (Castro-Castro et al., 2016; Genot and Gligorijevic, 2014; Lohmer et al., 2014; Murphy and Courtneidge, 2011). In contrast, little is known about the molecular and cellular processes that regulate large protrusion formation at sites of invadopodial breach, and in particular the mechanisms by which membrane is added to these protrusions within the tight confines of densely packed tissues. Using *C. elegans* AC invasion into the vulval tissue as a model, we found that in response to UNC-6 (netrin) secreted by the vulval tissue, the netrin receptor UNC-40 (DCC) directs lysosomes to the site of BM breach. Our results indicate that UNC-40 acts through the targeting t-SNARE SNAP-29 to trigger exocytosis of lysosomes to form an MMP-enriched invasive protrusion that dramatically increases in volume to create a large

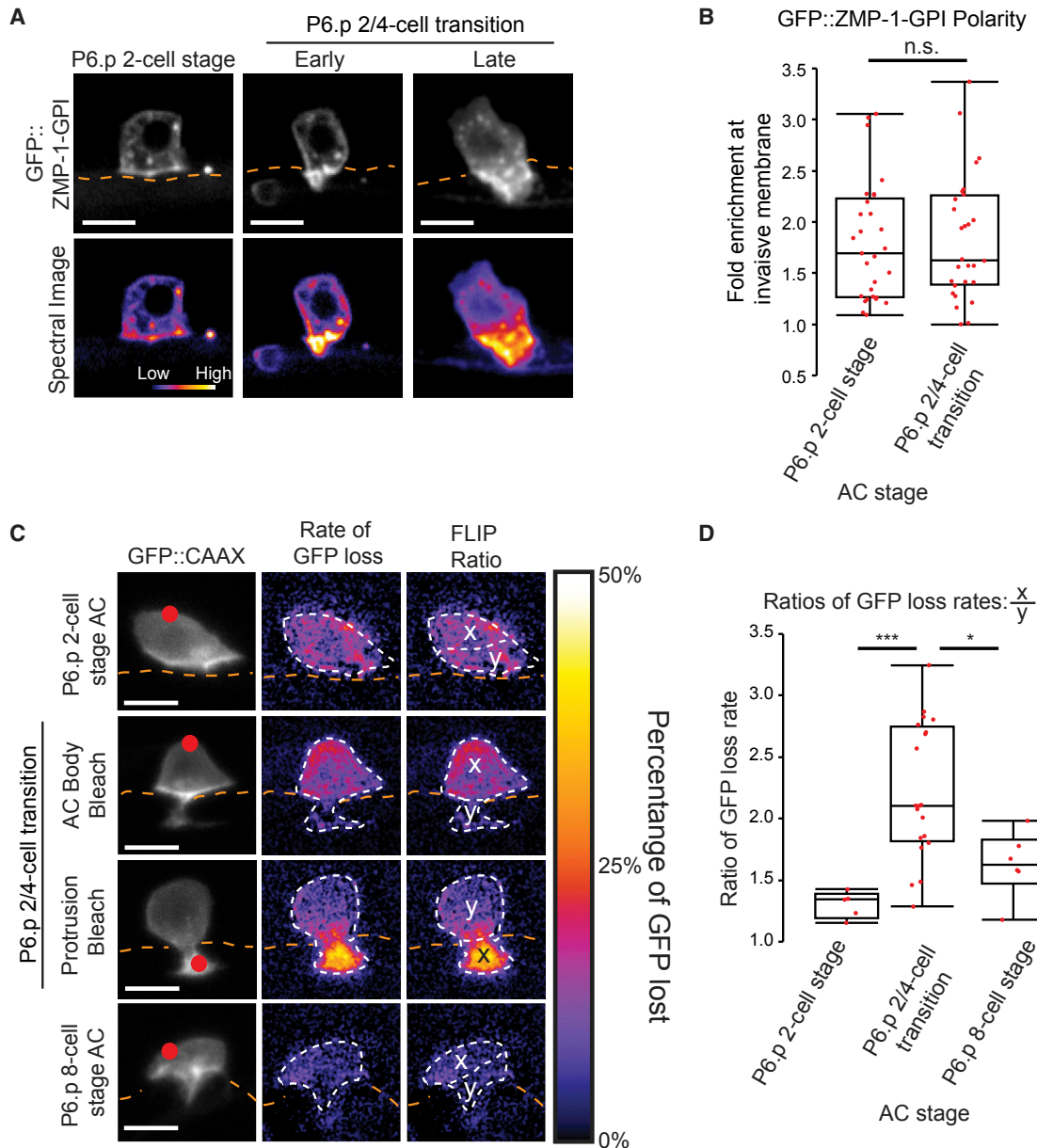


Figure 5. The Invasive Protrusion Is a Segregated Membrane Domain

(A) A reporter of ZMP-1 localization (*zmp-1>GFP::zmp-1-GPI*) (top) and corresponding spectral representation of fluorescence intensity (bottom) shows that ZMP-1 becomes highly concentrated in the invasive protrusion during its formation.

(B) Quantification of GFP::*ZMP-1-GPI* polarity before invasion (P6.p 2-cell stage, $n = 29$ animals) and in the invasive protrusion (P6.p 2/4-cell transition, $n = 28$ animals; n.s., not significant [$p > 0.05$], Student's *t* test).

(C) FLIP of AC membrane reporter (*cdh-3>GFP::CAAX*). Red dot indicates target of photobleaching (left). A smoothed spectral intensity map of percentage of GFP lost (center). The white dotted lines outline the AC. FLIP ratios (right) were determined by dividing the average loss in the region of photobleaching (X) by the average loss in the region of the AC not targeted (Y).

(D) FLIP ratios before invasion (P6.p 2-cell stage, $n = 5$ animals), during protrusion formation (targeting the invasive protrusion or the AC body, P6.p 2/4-cell transition, $n = 20$ animals), and after AC invasion (P6.p 8-cell stage, $n = 6$ animals) ($*p < 0.05$, $***p < 0.001$, one-way ANOVA with Tukey HSD *post-hoc* test). Scale bars, 5 μm . See also Figure S5.

opening in the BM and underlying vulval tissue. We show that the BM receptor dystroglycan clusters at the neck of the protrusion (the AC-BM interface) and forms a membrane diffusion barrier that enables protrusion growth. We further discovered that the protrusion is short lived: as it degraded and displaced the BM,

the dystroglycan-BM diffusion barrier was lost, and the protrusion retracted. Together these results define a netrin-directed pathway, which builds an invasive protrusion, a transient lysosome-derived membrane structure that is specialized to breach tissue barriers (Figure 7C).

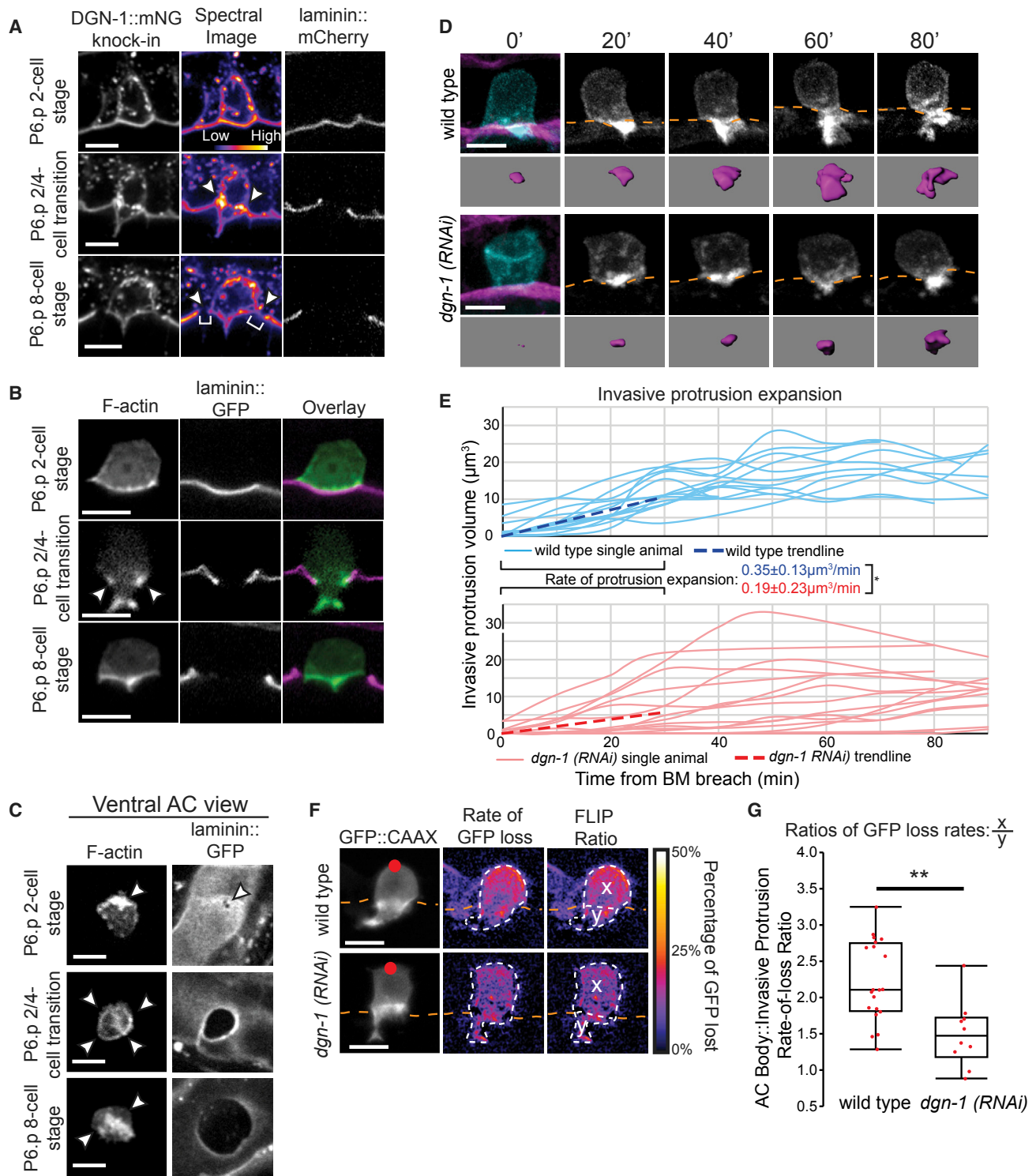


Figure 6. The BM Receptor Dystroglycan (DGN-1) Forms a Membrane Diffusion Barrier that Promotes Protrusion Formation

(A) ACs expressing *dgn-1::mNG* (*dgn-1* (*qy18*)) (left) and spectral representations of fluorescence intensity (center), with BM (laminin::GFP, right). DGN-1::mNG protein localizes to the invasive membrane before invasion (top), concentrates at the AC-BM interface (arrowheads) at the neck of the protrusion (middle), and is lost at this location (bottom) as the BM moves beyond the AC (brackets). The protrusion also retracts at this time.

(B) F-Actin (*cdh-3*>*mCherry::moesinABD*) similarly concentrates at the neck of the invasive protrusion at the AC-BM interface (arrowheads) during protrusion formation.

(legend continued on next page)

By using quantitative live-cell imaging during the stereotyped process of AC invasion, we discovered that invasive protrusion formation rapidly increases the AC's surface area by approximately 15%, far beyond the 2%–3% that a cell can stretch (Mohandas and Evans, 1994). We show that UNC-40/UNC-6 interactions polarize lysosomes, organelles that contribute lipids for membrane repair and neurite outgrowth (Arantes and Andrews, 2006; Reddy et al., 2001), to the breach site. As the invasive protrusion formed, it became enriched with the lysosomal protein LMP-1, and disruption of lysosomes inhibited protrusion formation, suggesting that lysosomes are used to form the protrusion. Finally, through a membrane-trafficking RNAi screen, we found that both the targeting SNARE SNAP-29 and the exocyst complex, which together mediate the docking, tethering, and fusion of exocytic vesicles (He and Guo, 2009), are expressed in the AC and promote invasive protrusion formation. Given that no protrusion formed in the absence of UNC-40 or UNC-6, our results suggest that the UNC-40/UNC-6 interaction acts through the t-SNARE SNAP-29 and the exocyst complex to facilitate exocytosis of lysosomes to form the invasive protrusion. In addition to membrane addition, lysosome exocytosis might contribute cathepsin proteases that could promote BM removal (Kirkegaard and Jäättelä, 2009). However, there are at least 43 genes encoding cathepsins in *C. elegans* (Xu et al., 2014) and extensive genetic and RNAi screens have not identified a role for cathepsins during AC invasion (Lohmer et al., 2016; Matus et al., 2010). Thus, if cathepsins do promote invasion they may function redundantly. Netrin-mediated membrane addition may be a common mechanism to construct invasive protrusions, as the vertebrate netrin-1 ligand is overexpressed in numerous metastatic cancers, and stimulates invasion in pancreatic, breast, colorectal, malignant melanoma, hepatocellular, and multiple brain tumors examined *in vitro* and *in vivo* (Ylivinkka et al., 2016).

The mechanisms that promote AC invasive protrusion formation have marked similarities to those guiding axon outgrowth and branching. The vertebrate UNC-40 receptor DCC interacts with the vertebrate homolog of SNAP-29 (the t-SNARE SNAP-25) to mediate exocytosis of membrane for axon outgrowth and branching (Winkle et al., 2014). Biochemical evidence suggests that this is mediated in part through the intracellular P3 domain of DCC, a domain shared with UNC-40 (Winkle et al., 2014; Ziel and Sherwood, 2010). Notably, DCC/SNAP-25 exocytosis is partially dependent on VAMP-7, a lysosomal V-SNARE (Winkle et al., 2014), suggesting that a similar lysosomal membrane source is also used in neurons. Further, the exocyst complex is required for axon outgrowth (Tojima

and Kamiguchi, 2015). Thus, the circuitry that directs membrane addition during axon outgrowth and AC invasion appears to be shared. This connection might reflect parallel functions of invasive protrusions and extending axons, as axon growth cones must also invade tissues during establishment of proper synaptic connections (Santiago-Medina et al., 2015).

Diffusion barriers are thought to help form and maintain specialized membrane domains in cells (Trimble and Grinstein, 2015). Several barriers have been described in plasma membranes, including the initial segment of axons, the phagocytic cup of macrophages, and the neck of budding yeast cells (Freeman et al., 2016; Nakada et al., 2003; Takizawa et al., 2000). Although the mechanisms that establish these barriers are poorly understood, it is thought that densely packed transmembrane and cytoskeletal proteins can act as molecular fences that contribute to barrier formation (Nakada et al., 2003; Trimble and Grinstein, 2015). We have discovered that the dystroglycan transmembrane BM receptor and F-actin concentrate in a ring around the neck of the protrusion at the AC-BM interface. FLIP and knockdown studies revealed that dystroglycan restricts the diffusion of an inner leaflet-anchored GFP protein between the protrusion and AC body, suggesting that dystroglycan forms a barrier that helps isolate the invasive protrusion. Loss of dystroglycan did not perturb the F-actin ring. The F-actin ring might help localize dystroglycan, as dystroglycan can be stabilized at specific cellular domains by anchoring to the cytoskeleton (Nakaya et al., 2013). F-actin has also been implicated as possibly stabilizing an integrin receptor diffusion barrier during phagocytosis (Freeman et al., 2016). Interestingly, rings of matrix adhesion proteins surround invadopodia in cancer cells, invasive podosomes in dendritic cells, and podosomes during sprouting angiogenesis (Branch et al., 2012; Gawden-Bone et al., 2010; Seano et al., 2014), suggesting that diffusion barriers might be a common mechanism to form protrusions that invade tissues.

Our results suggest that the primary function of the dystroglycan-BM diffusion barrier is to allow or maintain focused growth of the invasive protrusion. RNAi-mediated reduction of dystroglycan or the absence of the dystroglycan-BM barrier led to a loss of the protrusion or a dramatic reduction in protrusion size. Disassembly of the diffusion barrier may also trigger protrusion withdrawal; when the BM gap eventually widens beyond contact with the protrusion, the dystroglycan-BM barrier at the neck of the protrusion breaks down, and the protrusion retracts. The diffusion barrier at the neck of the invasive protrusion might have functional similarities with the barrier organized by a ring of septins at the neck of budding yeast, where this barrier restricts

(C) Ventral view of the AC-BM interface shows F-actin localization at the site of initial BM breach (top, arrowhead), in a ring (arrowheads) at the AC-BM contact site as the BM hole expands (middle), which is then lost (arrowheads) after the BM gap extends beyond the AC (bottom).

(D) Time-lapse images of AC protrusion formation in a uterine-specific RNAi strain with the AC membrane labeled by *cdh-3>mCherry::PLCδ^{PH}*, blue and grayscale, purple isosurface below; BM (laminin::GFP, magenta) position shown by orange dotted lines.

(E) AC protrusion volume over time for wild-type (blue) and *dgn-1* (RNAi) (red). Average expansion rates (dotted lines) ± SD for first 30 min of protrusion growth (n = 14 animals for wild-type, n = 16 animals for *dgn-1* (RNAi)); *p < 0.05, Student's t test). Wild-type controls were the same as in Figure 2D.

(F) FLIP of AC membrane reporter (*cdh-3>GFP::CAAX*). Red dot indicates target of photobleaching (left). A smoothed spectral intensity map of percentage of GFP lost (center). The white dotted lines outline the AC. FLIP ratios (right) were determined by dividing the average loss in the region of photobleaching (X) by the average loss in the region of the AC not targeted (Y).

(G) FLIP ratios for wild-type and *dgn-1* (RNAi). Controls were shared with the 2/4-cell transition data in Figure 5D (n = 20 animals for wild-type, n = 10 animals for *dgn-1* (RNAi)); **p < 0.01, Student's t test).

Scale bars, 5 μm. See also Figure S6.

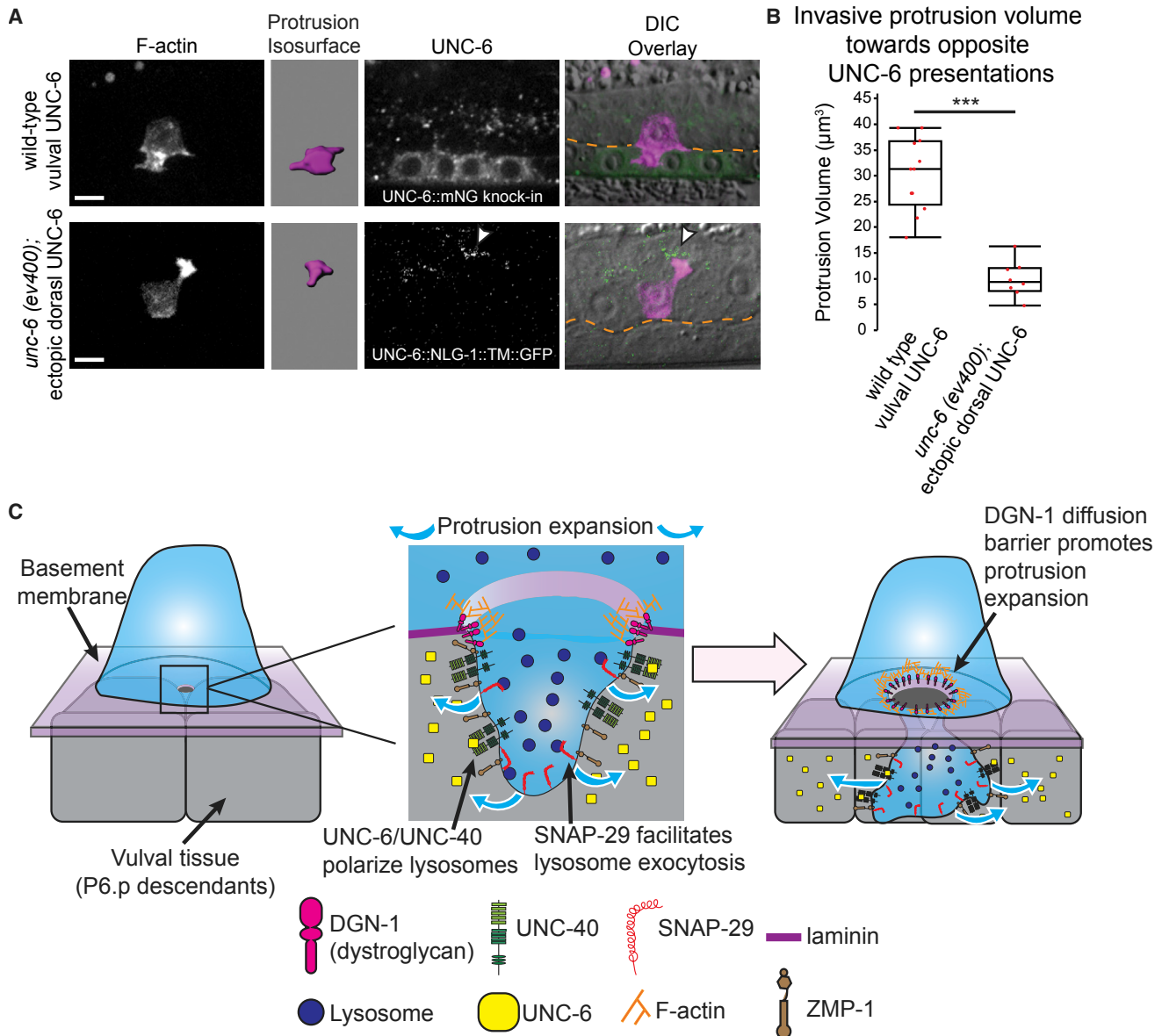


Figure 7. The BM Is a Scaffold for Protrusion Growth

(A) F-Actin (*cdh-3>mCherry::moesinABD*; left) marks the invasive protrusion (purple isosurface), UNC-6 (center), and overlay on DIC (right, BM position, orange). Endogenous UNC-6 (top) and dorsal uterine cell membrane-tethered UNC-6 (bottom, arrowhead). Scale bars, 5 μm .

(B) Maximum protrusion volume ($n = 12$ animals for wild-type, $n = 8$ animals for *unc-6(ev400)* with ectopic dorsal UNC-6; *** $p < 0.001$, Student's t test).

(C) Following invadopodial breach, the netrin receptor UNC-40 localizes to the breach site where it is activated by UNC-6 (netrin), which is secreted from in the central vulval cells (P6.p and its descendants). UNC-40 polarizes lysosomes, which add membrane to form the invasive protrusion through SNAP-29-mediated exocytosis. During protrusion growth GPI-anchored ZMP-1 concentrates in the invasive protrusion, and the BM receptor dystroglycan and F-actin localize to a ring at the AC-BM interface, forming a membrane diffusion barrier. This diffusion barrier allows focused membrane addition and expansion of the protrusion that clears an opening in the BM and vulval tissue allowing the AC to enter the vulval tissue.

growth to the new bud by focusing vesicle trafficking and membrane addition (Caudron and Barral, 2009). Dystroglycan's role in the AC diffusion barrier may be to physically restrict exocytosed membrane to allow for localized membrane expansion, or to locally restrict exocytosis to allow or facilitate deposition of new membrane only within the invasive protrusion. Because of the loss or dramatic reduction of the protrusion after dystroglycan knockdown, it was difficult to determine if the dystroglycan

diffusion barrier also maintains the lysosome-localized, membrane-bound protease ZMP-1. Given that lysosomes are also polarized by UNC-6/UNC-40 activity, and UNC-40 localizes to the invasive protrusion (Hagedorn et al., 2013), multiple mechanisms might function to maintain the unique molecular identity of the invasive protrusion.

Recent studies have shown that many mammalian cell types transiently expand in volume 10%–30% during mitosis (Son

et al., 2015; Zlotek-Zlotkiewicz et al., 2015). This expansion is not accompanied by an increase in mass, and thus dividing cells briefly decrease in density. A transient density decrease may also occur in the AC. It has been suggested that osmotic swelling might create strong pushing forces to allow mitotic cells to round in dense tissues (Stewart et al., 2011; Zlotek-Zlotkiewicz et al., 2015). Similarly, we suspect that focused membrane addition allows the invasive protrusion to penetrate initially small, confined gaps in tissues. Subsequent osmotic swelling coupled with the concentration of proteases and further membrane addition would then allow these gaps to be progressively widened by the expanding protrusion to clear a path for the invading cell. This idea is consistent with optical highlighting experiments demonstrating that the AC's invasive protrusion both degrades and physically displaces BM during invasion (Hagedorn et al., 2013).

Work examining cell migration and invasion in confined extracellular matrix and cellular *in vitro* and *in vivo* environments has revealed that cells harbor a remarkable repertoire of strategies to move through restrictive barriers, including shifts between amoeboid and mesenchymal migration, the ability to withstand nuclear envelope rupture, and even osmotic and nuclear-piston driven cell movement (Paul et al., 2017). Because of the challenges of examining cell size during the dynamic process of tissue invasion, however, it was not known if invasive cells can dynamically modulate membrane area and cell volume to enter tissues. Our work here establishes that an invasive cell can actively target membrane addition to the site of invasion and increase its volume locally to generate a large protrusion that promotes invasion through dense tissues. Given observations that cancer cells use single large protrusions to cross BMs into tissues (Hotary et al., 2006; Leong et al., 2014; Schoumacher et al., 2010), we expect this may be a common strategy for invading cells to breach tissue barriers.

STAR★METHODS

Detailed methods are provided in the online version of this paper and include the following:

- **KEY RESOURCES TABLE**
- **CONTACT FOR REAGENT AND RESOURCE SHARING**
- **EXPERIMENTAL MODEL AND SUBJECT DETAILS**
- **METHOD DETAILS**
 - Construction of Genomically-Edited Strains
 - Construction of Fusion Proteins
 - Microscopy and Image Acquisition
 - RNAi Experiments
 - Electron Microscopy
- **QUANTIFICATION AND STATISTICAL ANALYSIS**
 - Image Processing and AC Protrusion Volume
 - Analysis of AC Polarity
 - Colocalization Analysis
 - Fluorescence Loss in Photobleaching (FLIP)
 - Calculation of Basement Membrane Hole Opening Rates
 - Blinding and Unbiasing of Data
 - Statistical Analysis and Data Presentation

SUPPLEMENTAL INFORMATION

Supplemental Information includes six figures, three tables, and five movies and can be found with this article online at <https://doi.org/10.1016/j.devcel.2017.10.024>.

AUTHOR CONTRIBUTIONS

Conceptualization, K.M.N. and D.R.S.; Methodology, K.M.N. and Q.C.; Formal Analysis, K.M.N. and A.G.; Investigation, K.M.N., E.H., Z.W., D.P.K., and M.A.M.; Resources, K.M.N., Z.W., D.P.K., A.M.P., L.C.K., M.A.M., and Q.C.; Writing – Original Draft, K.M.N., E.H., K.L.G., and D.R.S.; Writing – Revised Draft, K.M.N. and D.R.S.; Supervision, D.R.S.; Funding Acquisition, E.H., K.L.G., A.M.P., B.G., and D.R.S.

ACKNOWLEDGMENTS

We thank Hanna Fares for organelle markers; Sam Johnson of the Duke University LCMF for imaging advice; Wei Zou for advice; and the University of Minnesota Caenorhabditis Genetics Center and National BioResource Project for strains used in this research. We thank Agnieszka Kawaska (info@illuscientia) for her work on the graphical abstract. E.H. is supported by postdoctoral fellowship 129351-PF-16-024-01-CSM from the American Cancer Society. K.G. is supported by postdoctoral fellowship GM121015-01 from the NIH. A.M.P. is supported by postdoctoral fellowship F32 GM115151 from the NIH. This work was supported by NIGMS R01 GM083071 to B.G. and NIGMS R01 GM079320 and NIGMS R35 MIRA GM118049 to D.R.S.

Received: May 30, 2017

Revised: September 19, 2017

Accepted: October 22, 2017

Published: November 20, 2017

REFERENCES

- Arantes, R.M.E., and Andrews, N.W. (2006). A role for synaptotagmin VII-regulated exocytosis of lysosomes in neurite outgrowth from primary sympathetic neurons. *J. Neurosci.* 26, 4630–4637.
- Armenti, S.T., Lohmer, L.L., Sherwood, D.R., and Nance, J. (2014). Repurposing an endogenous degradation system for rapid and targeted depletion of *C. elegans* proteins. *Development* 141, 4640–4647.
- Beatty, B.T., and Condeelis, J. (2014). Digging a little deeper: the stages of invadopodium formation and maturation. *Eur. J. Cell Biol.* 93, 438–444.
- Beerling, E., Ritsma, L., Vrisekoop, N., Derksen, P.W., and van Rheenen, J. (2011). Intravital microscopy: new insights into metastasis of tumors. *J. Cell Sci.* 124, 299–310.
- Bello, V., Moreau, N., Sirour, C., Hidalgo, M., Buisson, N., and Darrivière, T. (2015). The dystroglycan: nestled in an adhesome during embryonic development. *Dev. Biol.* 401, 132–142.
- Branch, K.M., Hoshino, D., and Weaver, A.M. (2012). Adhesion rings surround invadopodia and promote maturation. *Biol. Open* 1, 711–722.
- Castro-Castro, A., Marchesin, V., Monteiro, P., Lodillinsky, C., Rossé, C., and Chavrier, P. (2016). Cellular and molecular mechanisms of MT1-MMP-dependent cancer cell invasion. *Annu. Rev. Cell Dev. Biol.* 32, 555–576.
- Caudron, F., and Barral, Y. (2009). Septins and the lateral compartmentalization of eukaryotic membranes. *Dev. Cell* 16, 493–506.
- Dickinson, D.J., Pani, A.M., Heppert, J.K., Higgins, C.D., and Goldstein, B. (2015). Streamlined genome engineering with a self-excising drug selection cassette. *Genetics* 200, 1035–1049.
- Dyer, N., Rebollo, E., Domínguez, P., Elkhatib, N., Chavrier, P., Daviet, L., González, C., and González-Gaitán, M. (2007). Spermatocyte cytokinesis requires rapid membrane addition mediated by ARF6 on central spindle recycling endosomes. *Development* 134, 4437–4447.
- Edelstein, A., Amodaj, N., Hoover, K., Vale, R., and Stuurman, N. (2010). Computer control of microscopes using μ Manager. *Curr. Protoc. Mol. Biol. Chapter 14*, Unit14.20.

- Edelstein, A.D., Tsuchida, M.A., Amodaj, N., Pinkard, H., Vale, R.D., and Stuurman, N. (2014). Advanced methods of microscope control using μ Manager software. *J. Biol. Methods* **1**, e10.
- Fire, A., Xu, S., Montgomery, M.K., Kostas, S.A., Driver, S.E., and Mello, C.C. (1998). Potent and specific genetic interference by double-stranded RNA in *Caenorhabditis elegans*. *Nature* **391**, 806–811.
- Fraser, A.G., Kamath, R.S., Zipperlen, P., Martinez-Campos, M., Sohrmann, M., and Ahringer, J. (2000). Functional genomic analysis of *C. elegans* chromosome I by systematic RNA interference. *Nature* **408**, 325–330.
- Freeman, S.A., Goyette, J., Furuya, W., Woods, E.C., Bertozzi, C.R., Bergmeier, W., Hinz, B., van der Merwe, P.A., Das, R., and Grinstein, S. (2016). Integrins form an expanding diffusional barrier that coordinates phagocytosis. *Cell* **164**, 128–140.
- Friedl, P., and Wolf, K. (2010). Plasticity of cell migration: a multiscale tuning model. *J. Cell Biol.* **188**, 11–19.
- Gawden-Bone, C., Zhou, Z., King, E., Prescott, A., Watts, C., and Lucocq, J. (2010). Dendritic cell podosomes are protrusive and invade the extracellular matrix using metalloproteinase MMP-14. *J. Cell Sci.* **123**, 1427–1437.
- Genot, E., and Gligorijevic, B. (2014). Invadosomes in their natural habitat. *Eur. J. Cell Biol.* **93**, 367–379.
- Grant, B.D., and Donaldson, J.G. (2009). Pathways and mechanisms of endocytic recycling. *Nat. Rev. Mol. Cell Biol.* **10**, 597–608.
- Haerty, W., Artieri, C., Khezri, N., Singh, R.S., and Gupta, B.P. (2008). Comparative analysis of function and interaction of transcription factors in nematodes: extensive conservation of orthology coupled to rapid sequence evolution. *BMC Genomics* **9**, 399.
- Hagedorn, E.J., and Sherwood, D.R. (2011). Cell invasion through basement membrane: the anchor cell breaches the barrier. *Curr. Opin. Cell Biol.* **23**, 589–596.
- Hagedorn, E.J., Yashiro, H., Ziel, J.W., Ihara, S., Wang, Z., and Sherwood, D.R. (2009). Integrin acts upstream of netrin signaling to regulate formation of the anchor cell's invasive membrane in *C. elegans*. *Dev. Cell* **17**, 187–198.
- Hagedorn, E.J., Ziel, J.W., Morrissey, M.A., Linden, L.M., Wang, Z., Chi, Q., Johnson, S.A., and Sherwood, D.R. (2013). The netrin receptor DCC focuses invadopodia-driven basement membrane transmigration in vivo. *J. Cell Biol.* **201**, 903–913.
- Hagedorn, E.J., Kelley, L.C., Naegeli, K.M., Wang, Z., Chi, Q., and Sherwood, D.R. (2014). ADF/cofilin promotes invadopodial membrane recycling during cell invasion in vivo. *J. Cell Biol.* **204**, 1209–1218.
- Halfter, W., Oertle, P., Monnier, C.A., Camenzind, L., Reyes-Lua, M., Hu, H., Candiello, J., Labilloy, A., Balasubramani, M., Henrich, P.B., et al. (2015). New concepts in basement membrane biology. *FEBS J.* **282**, 4466–4479.
- Hall, D.H., Hartwig, E., and Nguyen, K.C.Q. (2012). Modern electron microscopy methods for *C. elegans*. *Methods Cell Biol.* **107**, 93–149.
- He, B., and Guo, W. (2009). The exocyst complex in polarized exocytosis. *Curr. Opin. Cell Biol.* **21**, 537–542.
- Hotary, K., Li, X.-Y., Allen, E., Stevens, S.L., and Weiss, S.J. (2006). A cancer cell metalloprotease triad regulates the basement membrane transmigration program. *Genes Dev.* **20**, 2673–2686.
- Jiu, Y., Jin, C., Liu, Y., Holmberg, C.I., and Jääntti, J. (2012). Exocyst subunits Exo70 and Exo84 cooperate with small GTPases to regulate behavior and endocytic trafficking in *C. elegans*. *PLoS One* **7**, e32077.
- Johnson, R.P., Kang, S.H., and Kramer, J.M. (2006). *C. elegans* dystroglycan DGN-1 functions in epithelia and neurons, but not muscle, and independently of dystrophin. *Development* **133**, 1911–1921.
- Kay, R.R., Langridge, P., Traynor, D., and Hoeller, O. (2008). Changing directions in the study of chemotaxis. *Nat. Rev. Mol. Cell Biol.* **9**, 455–463.
- Kelley, L.C., Wang, Z., Hagedorn, E.J., Wang, L., Shen, W., Lei, S., Johnson, S.A., and Sherwood, D.R. (2017). Live-cell confocal microscopy and quantitative 4D image analysis of anchor-cell invasion through the basement membrane in *Caenorhabditis elegans*. *Nat. Protoc.* **12**, 2081–2096.
- Kirkegaard, T., and Jäättelä, M. (2009). Lysosomal involvement in cell death and cancer. *Biochim. Biophys. Acta* **1793**, 746–754.
- Lecuit, T., and Pilot, F. (2003). Developmental control of cell morphogenesis: a focus on membrane growth. *Nat. Cell Biol.* **5**, 103–108.
- Lecuit, T., and Wieschaus, E. (2000). Polarized insertion of new membrane from a cytoplasmic reservoir during cleavage of the *Drosophila* embryo. *J. Cell Biol.* **150**, 849–860.
- Leong, H.S., Robertson, A.E., Stoletov, K., Leith, S.J., Chin, C.A., Chien, A.E., Hague, M.N., Ablack, A., Carmine-Simmen, K., McPherson, V.A., et al. (2014). Invadopodia are required for cancer cell extravasation and are a therapeutic target for metastasis. *Cell Rep.* **8**, 1558–1570.
- Lohmer, L.L., Kelley, L.C., Hagedorn, E.J., and Sherwood, D.R. (2014). Invadopodia and basement membrane invasion in vivo. *Cell Adh. Migr.* **8**, 246–255.
- Lohmer, L.L., Clay, M.R., Naegeli, K.M., Chi, Q., Ziel, J.W., Hagedorn, E.J., Park, J.E., Jayadev, R., and Sherwood, D.R. (2016). A sensitized screen for genes promoting invadopodia function in vivo: CDC-42 and Rab GDI-1 direct distinct aspects of invadopodia formation. *PLoS Genet.* **12**, e1005786.
- Matus, D.Q., Li, X.-Y., Durbin, S., Agarwal, D., Chi, Q., Weiss, S.J., and Sherwood, D.R. (2010). In vivo identification of regulators of cell invasion across basement membranes. *Sci. Signal.* **3**, ra35.
- Madsen, C.D., and Sahai, E. (2010). Cancer dissemination—lessons from leukocytes. *Dev. Cell* **19**, 13–26.
- Mohandas, N., and Evans, E. (1994). Mechanical properties of the red cell membrane in relation to molecular structure and genetic defects. *Annu. Rev. Biophys. Biomol. Struct.* **23**, 787–818.
- Morrissey, M.A., Hagedorn, E.J., and Sherwood, D.R. (2013). Cell invasion through basement membrane: the netrin receptor DCC guides the way. *Worm* **2**, e26169.
- Morrissey, M.A., Keeley, D.P., Hagedorn, E.J., McClatchey, S.T.H., Chi, Q., Hall, D.H., and Sherwood, D.R. (2014). B-LINK: a hemictin, plakin, and integrin-dependent adhesion system that links tissues by connecting adjacent basement membranes. *Dev. Cell* **31**, 319–331.
- Murphy, D.A., and Courtneidge, S.A. (2011). The “ins” and “outs” of podosomes and invadopodia: characteristics, formation and function. *Nat. Rev. Mol. Cell Biol.* **12**, 413–426.
- Nakada, C., Ritchie, K., Oba, Y., Nakamura, M., Hotta, Y., Iino, R., Kasai, R.S., Yamaguchi, K., Fujiwara, T., and Kusumi, A. (2003). Accumulation of anchored proteins forms membrane diffusion barriers during neuronal polarization. *Nat. Cell Biol.* **5**, 626–632.
- Nakaya, Y., Sukowati, E.W., and Sheng, G. (2013). Epiblast integrity requires CLASP and dystroglycan-mediated microtubule anchoring to the basal cortex. *J. Cell Biol.* **202**, 637–651.
- Nicot, A.-S., Fares, H., Payastre, B., Chisholm, A.D., Labouesse, M., and Laporte, J. (2006). The phosphoinositide kinase PIKfyve/Fab1p regulates terminal lysosome maturation in *Caenorhabditis elegans*. *Mol. Biol. Cell* **17**, 3062–3074.
- Paul, C.D., Mistriotis, P., and Konstantopoulos, K. (2017). Cancer cell motility: lessons from migration in confined spaces. *Nat. Rev. Cancer* **17**, 131–140.
- Raiborg, C., Wenzel, E.M., Pedersen, N.M., Olsvik, H., Schink, K.O., Schultz, S.W., Vietri, M., Nisi, V., Bucci, C., Brech, A., et al. (2015). Repeated ER-endosome contacts promote endosome translocation and neurite outgrowth. *Nature* **520**, 234–238.
- Reddy, A., Caler, E.V., and Andrews, N.W. (2001). Plasma membrane repair is mediated by Ca²⁺-regulated exocytosis of lysosomes. *Cell* **106**, 157–169.
- Rodríguez, A., Webster, P., Ortego, J., and Andrews, N.W. (1997). Lysosomes behave as Ca²⁺-regulated exocytic vesicles in fibroblasts and epithelial cells. *J. Cell Biol.* **137**, 93–104.
- Santiago-Medina, M., Gregus, K.A., Nichol, R.H., O'Toole, S.M., and Gomez, T.M. (2015). Regulation of ECM degradation and axon guidance by growth cone invadosomes. *Development* **142**, 486–496.
- Sato, K., Norris, A., Sato, M., and Grant, B.D. (2014). *C. elegans* as a model for membrane traffic. *WormBook*, 1–47, <https://doi.org/10.1895/wormbook.1.77.2>.
- Schindelin, J., Arganda-Carreras, I., Frise, E., Kaynig, V., Longair, M., Pietzsch, T., Preibisch, S., Rueden, C., Saalfeld, S., Schmid, B., et al. (2012). Fiji: an open-source platform for biological-image analysis. *Nat. Methods* **9**, 676–682.

- Schoumacher, M., Goldman, R.D., Louvard, D., and Vignjevic, D.M. (2010). Actin, microtubules, and vimentin intermediate filaments cooperate for elongation of invadopodia. *J. Cell Biol.* *189*, 541–556.
- Seano, G., Chiaverina, G., Gagliardi, P.A., di Blasio, L., Puliafito, A., Bouvard, C., Sessa, R., Tarone, G., Sorokin, L., Helley, D., et al. (2014). Endothelial podosome rosettes regulate vascular branching in tumour angiogenesis. *Nat. Cell Biol.* *16*, 931–941, 1–8.
- Shaner, N.C., Lambert, G.G., Chammas, A., Ni, Y., Cranfill, P.J., Baird, M.A., Sell, B.R., Allen, J.R., Day, R.N., Israelsson, M., et al. (2013). A bright monomeric green fluorescent protein derived from *Branchiostoma lanceolatum*. *Nat. Methods* *10*, 407–409.
- Sherwood, D.R., and Sternberg, P.W. (2003). Anchor cell invasion into the vulval epithelium in *C. elegans*. *Dev. Cell* *5*, 21–31.
- Sherwood, D.R., Butler, J.A., Kramer, J.M., and Sternberg, P.W. (2005). FOS-1 promotes basement-membrane removal during anchor-cell invasion in *C. elegans*. *Cell* *121*, 951–962.
- Son, S., Kang, J.H., Oh, S., Kirschner, M.W., Mitchison, T.J., and Manalis, S. (2015). Resonant microchannel volume and mass measurements show that suspended cells swell during mitosis. *J. Cell Biol.* *211*, 757–763.
- Stenmark, H. (2009). Rab GTPases as coordinators of vesicle traffic. *Nat. Rev. Mol. Cell Biol.* *10*, 513–525.
- Stewart, M.P., Helenius, J., Toyoda, Y., Ramanathan, S.P., Muller, D.J., and Hyman, A.A. (2011). Hydrostatic pressure and the actomyosin cortex drive mitotic cell rounding. *Nature* *469*, 226–230.
- Takizawa, P.A., DeRisi, J.L., Wilhelm, J.E., and Vale, R.D. (2000). Plasma membrane compartmentalization in yeast by messenger RNA transport and a septin diffusion barrier. *Science* *290*, 341–344.
- Tojima, T., and Kamiguchi, H. (2015). Exocytic and endocytic membrane trafficking in axon development. *Dev. Growth Differ.* *57*, 291–304.
- Trimble, W.S., and Grinstein, S. (2015). Barriers to the free diffusion of proteins and lipids in the plasma membrane. *J. Cell Biol.* *208*, 259–271.
- Wang, Z., Linden, L.M., Naegeli, K.M., Ziel, J.W., Chi, Q., Hagedorn, E.J., Savage, N.S., and Sherwood, D.R. (2014). UNC-6 (netrin) stabilizes oscillatory clustering of the UNC-40 (DCC) receptor to orient polarity. *J. Cell Biol.* *206*, 619–633.
- Winkle, C.C., McClain, L.M., Valtschanoff, J.G., Park, C.S., Maglione, C., and Gupton, S.L. (2014). A novel Netrin-1-sensitive mechanism promotes local SNARE-mediated exocytosis during axon branching. *J. Cell Biol.* *205*, 217–232.
- Xu, M., Liu, Y., Zhao, L., Gan, Q., Wang, X., and Yang, C. (2014). The lysosomal cathepsin protease CPL-1 plays a leading role in phagosomal degradation of apoptotic cells in *Caenorhabditis elegans*. *Mol. Biol. Cell* *25*, 2071–2083.
- Ylivinkka, I., Keski-Oja, J., and Hyytiäinen, M. (2016). Netrin-1: a regulator of cancer cell motility? *Eur. J. Cell Biol.* *95*, 513–520.
- Yurchenco, P.D. (2011). Basement membranes: cell scaffoldings and signaling platforms. *Cold Spring Harb. Perspect. Biol.* *3*, <https://doi.org/10.1101/cshperspect.a004911>.
- Ziel, J.W., and Sherwood, D.R. (2010). Roles for netrin signaling outside of axon guidance: a view from the worm. *Dev. Dyn.* *239*, 1296–1305.
- Ziel, J.W., Hagedorn, E.J., Audhya, A., and Sherwood, D.R. (2009). UNC-6 (netrin) orients the invasive membrane of the anchor cell in *C. elegans*. *Nat. Cell Biol.* *11*, 183–189.
- Zlotek-Zlotkiewicz, E., Monnier, S., Cappello, G., Le Berre, M., and Piel, M. (2015). Optical volume and mass measurements show that mammalian cells swell during mitosis. *J. Cell Biol.* *211*, 765–774.
- Zou, W., Yadav, S., DeVault, L., Nung Jan, Y., and Sherwood, D.R. (2015). RAB-10-Dependent membrane transport is required for dendrite arborization. *PLoS Genet.* *11*, e1005484.

STAR★METHODS

KEY RESOURCES TABLE

REAGENT or RESOURCE	SOURCE	IDENTIFIER
Bacterial and Virus Strains		
RNAi feeding strain	<i>Caenorhabditis</i> Genetics Center	HT115(DE3)
Vidal RNAi Library	Open Biosystems	ORF RNAi Collection V1.1
Ahringer RNAi Library	Source BioScience	<i>C. elegans</i> RNAi Collection (Ahringer)
Experimental Models: Organisms/Strains		
<i>C. elegans</i> wild-type strain	<i>Caenorhabditis</i> Genetics Center	WB-STRAIN:N2_(acestral)
<i>C. elegans unc-119</i> injection strain; Genotype: <i>unc-119 (ed4)</i> III	<i>Caenorhabditis</i> Genetics Center	WB Strain
<i>C. elegans unc-40</i> mutant with AC and BM markers; Genotype <i>unc-40 (e271)</i> I; <i>qyls166 (cdh-3>GFP::CAAX)</i> ; <i>qyls127 (</i>	This study	NK1916
<i>C. elegans</i> wild type strain with AC and BM markers; Genotype <i>qyls166 (cdh-3>GFP::CAAX)</i> III; <i>qyls127 (lam-1>laminin::mCherry)</i> V	Hagedorn et al., 2013	NK881
<i>C. elegans</i> wild type strain with LMP-1 marker; Genotype <i>qyls211 (cdh-3>LMP-1::GFP)</i>	Hagedorn et al., 2014	NK992
<i>C. elegans unc-40</i> mutant with LMP-1 marker; Genotype <i>qyls211 (cdh-3>LMP-1::GFP)</i> ; <i>unc-40 (e271)</i> I	This study	NK2300
<i>C. elegans unc-6</i> mutant with LMP-1 marker; Genotype <i>qyls211 (cdh-3>Imp-1::GFP)</i> ; <i>unc-6 (ev400)</i> X	This study	NK2299
<i>C. elegans</i> uterine-specific RNAi strain with AC and BM markers for time lapse analysis; Genotype <i>rrf-3 (pk1426)</i> II; <i>qyls10 (lamp-1>laminin::GFP)</i> IV; <i>rde-1 (ne219)</i> V; <i>qyls24 (cdh-3>mCherry::PLCδ^{PH})</i> ; <i>qyls102 (fos-1a>rde-1, myo-2>GFP)</i>	Morrissey et al., 2014	NK1316
<i>C. elegans</i> wild type strain with LMP-1 marker and UNC-6::mNG knock-in; Genotype <i>unc-6 (cp190 [unc-6::mNG^3xFLAG])</i> X; <i>qyls391 (zmp-1>Imp-1::mCherry)</i>	This study	NK2298
<i>C. elegans</i> strain with LMP-1 marker and ectopic UNC-6 expression; Genotype <i>unc-6 (ev400)</i> X; <i>qyls391 (zmp-1>Imp-1::mCherry)</i> ; <i>qyEx257 (zmp-5>unc-6::NLG-1TM::GFP)</i>	This study	NK1793
<i>C. elegans</i> strain with SNAP-29 transcriptional reporter; Genotype <i>qyEx549 (snap-29>GFP::SEC::ZF1)</i>	This study	NK2068
<i>C. elegans</i> strain with SNAP-29 marker; Genotype <i>qyls498 (lin-29>mCherry::snap-29)</i>	This study	NK2044
<i>C. elegans</i> strain with SNAP-29 marker; Genotype <i>qyls499 (lin-29>mCherry::snap-29)</i>	This study	NK2045
<i>C. elegans</i> strain with LMP-1 and SNAP-29 markers; Genotype <i>qyls498 (lin-29>mCherry::snap-29)</i> ; <i>qyls210 (cdh-3>LMP-1::GFP)</i>	This study	NK2283
<i>C. elegans</i> strain with AC and BM markers; Genotype <i>qyls23 (cdh-3>mCherry::PLCδ^{PH})</i> II; <i>qyls10 (lamp-1>laminin::GFP)</i> IV	Ziel et al., 2009	NK361

(Continued on next page)

Continued

REAGENT or RESOURCE	SOURCE	IDENTIFIER
<i>C. elegans</i> strain with <i>exoc-8</i> mutation and AC and BM markers; Genotype <i>exoc-8 (ok2523)</i> I; <i>qyls23 (cdh-3>mCherry::PLCδ^{PH})</i> II; <i>qyls10 (lam-1>laminin::GFP)</i> IV	This study	NK1674
<i>C. elegans</i> strain with ZMP-1-GPI marker; Genotype <i>qyEx260 (zmp-1>GFP::ZMP-1-GPI)</i>	This study	NK1123
<i>C. elegans</i> strain with CAAX marker; Genotype <i>qyls509 (cdh-3>GFP::CAAX)</i>	This study	NK2099
<i>C. elegans</i> strain with mNG knock-in at <i>dgn-1</i> locus and BM marker; Genotype <i>qyls127 (lam-1>laminin::mCherry)</i> V; <i>dgn-1 (qy18 [dgn-1::mNG])</i> X	This study	NK2150
<i>C. elegans</i> strain with F-actin and BM markers; Genotype <i>qyls50 (cdh-3>mCherry::moesinABD)</i> V; <i>qyls7 (lam-1>laminin::GFP)</i> X	Ziel et al., 2009	NK972
<i>C. elegans</i> strain with F-actin marker and UNC-6 mNG knock-in; Genotype <i>qyls50 (cdh-3>mCherry::moesinABD)</i> V; <i>unc-6 (cp190 [unc-6::mNG\wedge3xFLAG])</i> X	This study	NK2031
<i>C. elegans</i> strain with F-actin marker and ectopic UNC-6 expression; Genotype <i>qyls50 (cdh-3>mCherry::moesinABD)</i> V; <i>unc-6 (ev400)</i> X; <i>qyEx257 (zmp-5>unc-6::NLG-1TM::GFP)</i>	Wang et al., 2014	NK2302
<i>C. elegans</i> strain with RAB-5 marker; Genotype <i>qyls257 (cdh-3>mCherry::rab-5)</i>	Hagedorn et al., 2014	NK1108
<i>C. elegans</i> strain with RAB-7 marker; Genotype <i>qyls252 (cdh-3>mCherry::rab-7)</i>	Hagedorn et al., 2014	NK1100
<i>C. elegans</i> strain with RAB-11 marker; Genotype <i>qyls205 (cdh-3>mCherry::rab-11)</i>	Hagedorn et al., 2014	NK986
<i>C. elegans</i> strain with CYTB-5.1 marker; Genotype <i>qyEx72 (cdh-3>cytb-5.1::GFP)</i>	This study	NK530
<i>C. elegans</i> strain with AMAN-2 marker; Genotype <i>qyEx73 (cdh-3>aman-2::GFP)</i>	This study	NK531
<i>C. elegans</i> strain with CUP-5 marker; Genotype <i>qyls409 (cdh-3>GFP::cup-5)</i>	Hagedorn et al., 2014	NK1616
<i>C. elegans</i> strain for RNAi screen; Genotype <i>rrf-3 (pk1426)</i> II; <i>qyls166 (cdh-3>GFP::CAAX)</i> III; <i>qyls127 (lam-1>laminin::mCherry)</i> V	This study	NK1339
<i>C. elegans</i> strain with UNC-40 marker; Genotype <i>qyls66 (cdh-3>unc-40::GFP)</i> X	Ziel et al., 2009	NK388
<i>C. elegans</i> strain with SEC-5 YFP knock-in; Genotype <i>sec-5 (xn51 [sec-5-zf1-YFP + unc-119(+)])</i> II	Armenti et al., 2014	FT1523
<i>C. elegans</i> strain with SEC-15 marker; Genotype <i>sec-15 (xnSi34 [sec-15>sec-15::YFP + unc-119(+)])</i> II	Armenti et al., 2014	FT1379
<i>C. elegans</i> strain with EXOC-8 marker; Genotype <i>qyEx517 (cdh-3>exoc-8::GFP)</i>	This study	NK1944
<i>C. elegans</i> strain with SEC-5 marker; Genotype <i>qyEx519 (cdh-3>sec-5::GFP)</i>	This study	NK1946
<i>C. elegans</i> strain with SEC-15 marker; Genotype <i>qyls484 (cdh-3>sec-15::GFP)</i>	This study	NK1950
<i>C. elegans</i> strain with EXOC-7 marker; Genotype <i>qyEx520 (cdh-3>exoc-7::GFP)</i>	This study	NK1947

(Continued on next page)

Continued

REAGENT or RESOURCE	SOURCE	IDENTIFIER
<i>C. elegans</i> strain with <i>exoc-8</i> mutant and UNC-40 marker; Genotype <i>exoc-8 (ok2523)</i> I; <i>qyls66 (cdh-3>unc-40::GFP)</i> X	This study	NK2036
<i>C. elegans</i> strain with <i>exoc-8</i> mutant and LMP-1 marker; Genotype <i>exoc-8 (ok2523)</i> I; <i>qyls166 (cdh-3>GFP::CAAX)</i> X <i>qyls391 (zmp-1>Imp-1::mCherry)</i>	This study	NK2003
<i>C. elegans</i> strain with LMP-1 and ZMP-1-GPI markers; <i>qyEx260 (zmp-1>GFP::ZMP-1-GPI)</i> ; <i>qyls391 (zmp-1>Imp-1::mCherry)</i>	This study	NK2276
<i>C. elegans</i> strain with PAT-3 and BM marker; Genotype <i>qyls42 (pat-3>pat-3::GFP, genomic ina-1)</i> IV; <i>qyls127 (lam-1>laminin::mCherry)</i> V	Hagedorn et al., 2009	NK572
<i>C. elegans</i> strain with dnIntegrin; Genotype <i>qyls15 (zmp-1>HA-βtail)</i>	Hagedorn et al., 2009	NK261
<i>C. elegans</i> strain with <i>ina-1</i> mutation and CAAX marker; Genotype <i>ina-1 (gm39)</i> III; <i>qyls509 (cdh-3>GFP::CAAX)</i>	This study	NK2119
<i>C. elegans</i> strain with <i>unc-40</i> mutation and SNAP-29 marker; Genotype <i>unc-40 (e271)</i> I; <i>qyls499 (lin-29>mCherry::snap-29)</i>	This study	NK2063
Oligonucleotides		
See Table S3 for oligonucleotide sequences	This study	N/A
Recombinant DNA		
Plasmid for CRISPR/Cas9 sgRNA	Dickinson et al., 2015	pDD162
GFP::CAAX plasmid	Hagedorn et al., 2013	pSA129
pBlueScript with <i>cdh-3</i> promoter and GFP	This study	pBS-cdh3-GFP
Plasmid for CRISPR/Cas9 selection cassette and homology arms	Dickinson et al., 2015	pDD240
pBlueScript with <i>zmp-1>mCherry</i>	This study	pBS-zmp1-mCh
Plasmid containing <i>aman-2::GFP</i>	Hanna Fares	pHD93
Plasmid containing <i>cytb-5.1::GFP</i>	Hanna Fares	pHD189
Plasmid containing <i>cdh-3</i> AC promoter	Hagedorn et al., 2014	pPD107.94
RNAi empty vector control	Fire et al., 1998	L4440
Software and Algorithms		
Fiji	Schindelin et al., 2012	ImageJ 1.51f, http://fiji.sc/
Photoshop	Adobe	Version CC 2015
Imaris	Bitplane, Inc	Version 7.6.5
Illustrator	Adobe	Version CC 2015
JMP	SAS	Version 12.0
μmanager	Edelstein et al., 2014	Version 1.4, https://micro-manager.org/
Excel	Microsoft	Version 2010

CONTACT FOR REAGENT AND RESOURCE SHARING

Further information and requests for resources and reagents should be directed to and will be fulfilled by the Lead Contact, David R. Sherwood (david.sherwood@duke.edu).

EXPERIMENTAL MODEL AND SUBJECT DETAILS

C. elegans strains were maintained on standard NGM media and fed *E. coli* OP50. For RNAi experiments, wild type controls were fed *E. coli* HT115(DE3) containing L4440 (see RNAi experiments, [STAR Methods](#)). Unless otherwise noted, all strains were maintained at 20°C. All animals scored were hermaphrodites during the L3 stage when the anchor cell (AC) invades. AC invasion was precisely

staged in reference to VPC divisions and gonad development as previously described (Sherwood et al., 2005). Briefly, the AC is positioned over the central P6.p vulval precursor cell prior to invasion in the early L3 larval stage. During the mid L3 stage the P6.p cell divides once (P6.p 2-cell stage). At the late P6.p 2-cell stage the AC initiates BM breach (near the time with the distal tip cells of the gonad arm begin migrating dorsally). At the P6.p 2-to-4-cell transition (when the P6.p daughters divide) the AC protrusion forms and clears an opening in the basement membrane and extends around and between the P6.p vulval precursor cell descendants. At the early P6.p 4-cell stage (mid-to-late L3 stage), the protrusion retracts back into the AC (Figure 1A).

METHOD DETAILS

Construction of Genomically-Edited Strains

Endogenous tagging of the C-terminus of *unc-6* with the mNG::3xFLAG sequence was accomplished using CRISPR/Cas9-mediated genome editing using a homologous repair template containing 500bp homology arms, the mNG::3XFLAG, and a selection markers as described previously (Dickinson et al., 2015). For *unc-6* we used a guide RNA (sgRNA) with a targeting sequence of 5'-TATCTGTGTGACGTAATCTCTGG-3'. GFP was similarly knocked into the *dgn-1* locus by CRISPR/Cas9-triggered homologous recombination using a homologous repair template with a selectable marker, GFP, and 1.7kb homology arms at the HindIII site 7 amino acids upstream of the stop codon (Johnson et al., 2006) using two sgRNA targeting sequences, 5'-GATGAAGCATGTcCGA GACGCGG-3' (antisense) and 5'-GCCAGCAACTCTCCGCGTCTCGG-3' (sense). Silent mutations were introduced into the homology arms using site directed mutagenesis. See Table S3 for homology arm oligonucleotide primer sequences. For construction of both genome edited strains, the sgRNA targeting sequences were cloned into the pDD162 Cas9-sgRNA expression vector for *C. elegans*. The homologous repair template and Cas9-sgRNA plasmids were coinjected into the gonad of young adult N2 worms. Animals that were recombinant were identified in the F3 offspring of injected animals based on the presence of selectable markers (dominant-negative *sqt-1 rol* phenotype and hygromycin resistance). Following strain isolation, the selectable markers were removed from the genome through Cre-Lox recombination and proper genome editing was confirmed by amplification and sequencing of the edited region.

Construction of Fusion Proteins

In text, figures, and methods, we use ">" to denote linkage to a promoter and "::" to denote linkages of open reading frames.

GFP::CAAX was amplified from pSA129 and then cloned into pBlueScript containing 1.5kb AC-regulatory region of the *C. elegans cdh-3* promoter at Sall and SacI sites (see Table S3 for oligonucleotide sequences) (Sherwood et al., 2005).

The AC-specific endoplasmic reticulum marker *cdh-3>cytb-5.1::GFP* was constructed by PCR fusion. A 3.0kb fragment of the full length *cytb-5.1* sequence, GFP, and the *let-858* 3' UTR from pHD189 was fused with a 2.2kb fragment of the *cdh-3* promoter region amplified from pPD107.94 (see Table S3 for oligonucleotide sequences).

The AC-specific Golgi apparatus marker *cdh-3>aman-2::GFP* was constructed by PCR fusion. A 2.3kb fragment of *aman-2*, GFP, and the *let-858* 3' UTR from pHD93 was fused with a 2.2kb fragment of the *cdh-3* promoter region amplified from pPD107.94 (see Table S3 for oligonucleotide sequences).

Fusion of the *lin-29* promoter (5.4kb, see Table S3) to the *snap-29* open reading frame starting from the ATG translation start site amplified from *C. elegans* genomic DNA (1.3kb) and mCherry from a modified pBlueScript (0.9kb) was accomplished by Gibson assembly using pBlueScript as a backbone (3.6kb).

Exocyst components (*exoc-8*, *exoc-7*, *sec-15*, and *sec-5*) fused to GFP previously (Zou et al., 2015) were amplified from their corresponding plasmids and fused to 1.7kb of the *cdh-3* promoter amplified from pBlueScript by PCR fusion (see Table S3 for oligonucleotide sequences).

A 0.9kb fragment of LMP-1 encompassing the complete open reading frame from the ATG translation start site was amplified using genomic DNA (see Table S3 for oligonucleotide sequences) was cloned into pBlueScript containing *zmp-1>mCherry* at AgeI and PacI sites to generate *zmp-1>Imp-1::mCherry*.

The *snap-29>GFP* transcriptional reporter was generated from 1.4kb of sequence 5' of the *snap-29* transcription start site expressed as an extrachromosomal array (see Table S3 for oligonucleotide sequences).

The *zmp-1>GFP::zmp-1-GPI* construct was generated by amplifying the *zmp-1* GPI membrane targeting sequence (an 84 base pair fragment encompassing the final 28 amino acids of *zmp-1*; see Table S3 for oligonucleotide sequences) from genomic DNA and cloning this fragment into pBlueScript containing GFP using EcoRV and NotI sites. The resulting GFP::GPI sequence was then amplified with oligonucleotides for GFP::GPI (forward) and the *unc-54* 3' UTR (reverse) and joined to the 2.7kb of sequence 5' of the *zmp-1* transcription start site and the *zmp-1* signal sequence (first 66 amino acids) by PCR fusion.

All constructs were injected into the syncytial gonads of young adult *unc-119* (*ed4*) hermaphrodites along with 50ng/ μ L *unc-119* rescue DNA, 50ng/ μ L pBSSk(-), and 50ng/ μ L EcoRI-digested salmon sperm DNA. F1 animals were selected for recovery of wild type animal movement (rescue of the *unc-119* phenotype), and stable lines were selected based on transmission of stable extrachromosomal transgenes into the F2 generation. Integrated lines were generated by gamma irradiation as previously described (Sherwood et al., 2005). Briefly, approximately 50 young adult hermaphrodites carrying the extrachromosomal transgenes were irradiated with 3800rad of γ irradiation from Cesium-137 and rescued to plates to produce progeny. F1 animals (5 per parent) exhibiting rescue of the *unc-119* phenotype were singled to NGM plates. Plates that showed 100% rescue of the *unc-119* phenotype in the F2 were considered stable integrants, evaluated for transgene expression, and then backcrossed into strain N2.

Microscopy and Image Acquisition

All time-lapse and polarity images were acquired using an EM-CCD or Orca-R² camera (Hamamatsu Photonics) and a spinning disk confocal microscope (CSU-10, Yokogawa) mounted on an upright AxioImager microscope (Carl Zeiss) with a Plan-APOCHROMAT 100x/1.4 oil differential interference contrast objective controlled by μ manager software (version 1.4) (Edelstein et al., 2010). Time-lapse acquisition was performed as described previously (Kelley et al., 2017). Synchronized L3 hermaphrodites were anesthetized in 0.2% tricaine and 0.02% levamisole in M9 for 20 minutes and then transferred to 5% noble agar pads. The cover slip was sealed with VALAP and worms were imaged at 23°C for two hours. For protrusion analysis, confocal stacks of marked ACs with protrusions (23 optical slices, each at 0.5 μ m thickness) were acquired every five minutes to avoid photobleaching. Some time-lapses were acquired every minute to construct movies with better temporal resolution.

For single-timepoint AC snapshots and all scoring of AC invasion, worms were anesthetized on 5% noble agar pads with 0.01M sodium azide. Fluorescence images of the AC were acquired as confocal z-stacks with 0.5 μ m optical slices spanning the entire cell.

Images of ACs on *rab-11.1* (RNAi) and wild type controls (Figure S3A) were acquired on a Zeiss AxioImager A1 microscope with a 100x plan-apochromat objective and Zeiss AxioCam MRm CCD camera controlled by Zeiss Axiovision software (Zeiss Microimaging).

RNAi Experiments

RNAi was delivered by feeding worms *E. coli* feeding strain HT115(DE3) expressing double-stranded RNA (Fire et al., 1998). Bacteria harboring an empty RNAi vector (L4440) was used as a negative control for all RNAi experiments. RNAi clones targeting *C. elegans* genes originated from the *C. elegans* ORF-RNAi Collection V1.1 (Open Biosystems) and an RNAi library constructed by the Ahinger lab (Fraser et al., 2000). Transcription of RNAi vector expression was induced with 1mM Isopropyl β -D-1-thiogalactopyranoside (IPTG) and cultures were plated on plates containing NGM and topical application of 5 μ L each of 30mg/mL carbenicillin and 1M IPTG. Synchronized L1-arrested larvae were plated on the RNAi-expressing HT115(DE3) and grown for 40-48 hours at 16°C before scoring. RNAi that produced phenotypes were sequenced to verify correct insert.

For uterine-specific RNAi experiments, the strain NK1316 was utilized (Haerty et al., 2008; Hagedorn et al., 2009). The strain harbors mutations in *rrf-3* (*pk1426*), an RNA-directed RNA polymerase whose loss sensitizes the worms to RNAi, as well as *rde-1* (*ne219*), an argonaute protein required for RNAi (Hagedorn et al., 2009). Expression of *rde-1* in the somatic uterine cells (*fos-1a>rde-1*) specifically restores RNAi in the uterine cells.

Electron Microscopy

Transmission electron micrographs were acquired in serial sections as described previously (Hall et al., 2012; Morrissey et al., 2014). L3 worms were anesthetized with 1% phenyl-isopropanol in fixative buffer and then fixed in 2.5% glutaraldehyde, 1.5% paraformaldehyde in 0.1M Na-cacodylate buffer. Worms were cut open in the head or tail region and incubated for 2.5 hours. Samples were then washed three times in 0.1M Na-cacodylate buffer, stained in 1% UAC in 0.1M Na-acetate buffer, and then washed once in Na-acetate buffer and twice in Na-cacodylate buffer. Worms were then embedded in 3% agarose and dehydrated in ethanol. Samples were then embedded in Embed812 resin and propylene oxide solutions followed by embedding in 100% Embed812 resin for two days. Samples were then incubated at 60°C for 2 days. Longitudinal sections were cut across the gonad to allow for evaluation of the tissue to establish precise developmental stage and to identify the anchor cell. Images were then acquired on a Philips CM12 transmission electron microscope.

QUANTIFICATION AND STATISTICAL ANALYSIS

Image Processing and AC Protrusion Volume

Acquisition of images is described above in "Microscopy and Image Acquisition". Acquired confocal z-stack images were processed with Fiji (ImageJ 1.51f) and Photoshop (CC 2015; Adobe) (Schindelin et al., 2012). Time-lapse analysis and 3D reconstructions of protrusion formation and growth were built from confocal z-stacks, analyzed, and exported using Imaris 7.6.5 (Bitplane, Inc). Importantly, in some instances out-of-focus fluorescence from intense membrane signal above the protrusion was captured in slices. This signal was clearly distinguished and excluded from the relevant slices (and thus volume analysis), but this out-of-focus fluorescence in some instances appeared to broaden and obscure the edges of the protrusion in 3D Imaris renderings. Supplementary movies were exported at 20 frames per second as.mp4 files using the 3D reconstructions of time-lapse data in the Imaris 7.6.5 Animation module with key frames designated every 20 minutes.

Invasive protrusion volume and total AC volume were calculated as previously described by our laboratory (Kelley et al., 2017). In time-lapses, AC protrusion volume was calculated by hand-tracing the protrusion (the region of the AC extending below the BM) in each slice to generate an isosurface for each time point in Imaris 7.6.5. All rates of invasive protrusion expansion were calculated over the first thirty minutes of time-lapse image series following BM breach (images collected every five minutes, see above), as this was the time period of maximal growth of the invasive protrusion. The difference in protrusion volume at the time of initial breach was subtracted from the size of the protrusion thirty minutes after breach; this difference was then divided by the time that transpired (30 minutes) to obtain a rate of expansion for each animal observed.

For surface area and volume measurements of the entire AC, isosurfaces were generated in Imaris by manual thresholds of fluorescence intensity using 0.300 μ m surface detail. The volume of the invasive protrusion in these comparisons (Figure S1C) was then

calculated by using the Imaris isosurface slicer tool to cut the AC isosurface at the AC-BM junction, thus separating the AC from the invasive protrusion. In comparisons across stages of invasion (P6.p 2-cell, P6.p 2/4-cell transition, and P6.p 4-cell stages), AC surface area or volume was normalized to average AC surface area or volume for ACs of the corresponding genotype before invasion (P6.p 2-cell stage). In dominant negative integrin (*zmp-1>HA-βtail*) animals, AC invasion is delayed, so data were collected from ACs that breached the BM at the P6.p 8-cell stage before the BM hole expanded beyond the AC.

Three strains were used for invasive protrusion analysis: NK881 (AC labeled with *qyls166 (cdh-3>GFP::CAAX)*, Figure 1), NK361 (AC labeled with *qyls24 (cdh-3>mCherry::PLCδ^{PH}*, Figure 4), and NK1316 (uterine-specific RNAi line with the AC labeled with *qyls24 (cdh-3>mCherry::PLCδ^{PH}*, Figures 2, 3, and 6). We found that strains NK881 and NK361 showed slightly faster rates of protrusion formation (0.47 and 0.48 μm³/min) while the uterine specific line was a little slower (0.35 μm³/min), although the rate was not statistically different ($p > 0.05$, Student's t test).

Analysis of AC Polarity

AC polarity measurements were generated from background-subtracted sum projections of the AC using Fiji. Polarity was measured using a 5-pixel wide line tracing the invasive membrane (P6.p 2-cell stage) or invasive protrusion membrane (P6.p 2/4-cell transition) from centermost image slices. This value was then divided by the mean intensity of a 5-pixel wide line tracing the apical membrane of the AC in its centermost slice to determine fold enrichment of fluorescently tagged proteins at the invasive cell membrane. ImageJ macros that semi-automate this method of polarity measurement follows (this can be downloaded at <https://sites.duke.edu/sherwoodlab/protocols/>):

Anchor Cell Polarity for the P6.p 2-Cell Stage

```

1. /* Anchor Cell Polarity at the P6.p 2-cell stage
2. * this a macro to quickly calculate polarity in the AC for a one-channel image. It will return
3. * two lines of results.
4. *
5. * Line 1 of the results is the apical domain of the AC available upon request.
6. * Line 2 of the results is the invasive membrane
7. *
8. * IMPORTANT: Change the code in line 15 to match proper pixel size:
9. * IMPORTANT: Ensure freehand lines are 5-pixels wide. The code on line 33 does not work for
10. * all versions of Fiji
11. */
12. image=getTitle;
13. n=nSlices;
14. run("Set Measurements...", "area mean integrated redirect=None decimal=3");
15. run("Properties...", "channels=1 slices=n frames=1 unit=μm pixel_width=.15 pixel_height=.15 voxel_depth=0.5000000");
16. roiManager("Reset");
17. //calculate polarity of a single slice of the AC
18. waitForUser("select the center-most slice of the AC");
19. run("Duplicate...", "title=slice");
20. selectWindow("slice");
21. run("Subtract Background...", "rolling=100");
22. //run("Brightness/Contrast...");
23. resetMinAndMax();
24. selectWindow("slice");
25. setTool("point");
26. waitForUser("mark the AC");
27. run("To Selection");
28. run("Out [-]");
29. run("Out [-]");
30. run("Out [-]");
31. run("Out [-]");
32. run("Out [-]");
33. setTool("freeline");
34. setLineWidth(5);
35. waitForUser("draw a line along the apical membrane.");
36. run("Measure");
37. waitForUser("draw a line along the invasive membrane.");
38. run("Measure");
39. run("Close All");

```

Anchor Cell Polarity for P6.p 2-to-4 Cell Transition

```

1. /* this a macro to quickly calculate polarity in the AC for a one-channel image. It will return
2. * three lines of results.
3. * Polarity on each line is AC first, then IM
4. * Line 1 is the apical domain of the AC
5. * Line 2 is the invasive membrane
6. * Line 3 is a second run of the invasive membrane (if required - usually just for the protrusion)
7. * Line 4 is a third run of the invasive membrane (if required)
8. * IMPORTANT - Change the code in line 15 to match proper pixel size for your image:
9. * IMPORTANT - Ensure freehand lines are 5-pixels wide. The code on line 41 does not work
10. * for all versions of Fiji
11. */
12. image=getTitle;
13. n=nSlices;
14. run("Set Measurements...", "area mean integrated redirect=None decimal=3");
15. run("Properties...", "channels=1 slices=n frames=1 unit= $\mu\text{m}$  pixel_width=.15 pixel_height=.15 voxel_depth=0.5000000");
16. roiManager("Reset");
17. run("Subtract Background...", "rolling=100 stack");
18. //calculate polarity of a single slice of the AC
19. waitForUser("select the center-most slice of the AC");
20. run("Duplicate...", "title=slice");
21. selectWindow("slice");
22. //run("Brightness/Contrast...");
23. resetMinAndMax();
24. selectWindow("slice");
25. setTool("point");
26. waitForUser("mark the AC");
27. run("To Selection");
28. run("Out [-]");
29. run("Out [-]");
30. run("Out [-]");
31. run("Out [-]");
32. run("Out [-]");
33. setTool("reeline");
34. setLineWidth(5);
35. waitForUser("draw a line along the apical membrane.");
36. run("Measure");
37. selectWindow(image);
38. waitForUser("select the center-most slice of the protrusion");
39. run("Duplicate...", "title=protrusion");
40. //run("Brightness/Contrast...");
41. resetMinAndMax();
42. selectWindow("protrusion");
43. setTool("point");
44. waitForUser("mark the AC");
45. run("To Selection");
46. run("Out [-]");
47. run("Out [-]");
48. run("Out [-]");
48. run("Out [-]");
49. run("Out [-]");
50. setTool("freeline");
51. waitForUser("draw a line along the invasive membrane.");
52. run("Measure");
53. roiManager("Add");
54. roiManager("Show All");
55. //run("Select None");
56. waitForUser("draw another invasive membrane line if needed; if not, just click OK");
57. run("Measure");

```

```

58. roiManager("Add");
59. roiManager("Show All");
60. waitForUser("draw a third invasive membrane line if needed; if not, just click OK");
61. run("Measure");
62. run("Close All");

```

Colocalization Analysis

Colocalization analysis was performed in Fiji as described previously by our laboratory (Wang et al., 2014). The centermost slice of the AC was selected from confocal z-stacks with signal from two fluorophores. A 3-pixel wide line was drawn through the AC membrane and the absolute intensity of each fluorophore was measured every 0.15 μm along this line (reported by Fiji as Integrated Density). The intensity profile for each fluorophore was then normalized to the maximum measured intensity of that fluorophore along the line.

Fluorescence Loss in Photobleaching (FLIP)

Images from fluorescence loss in photobleaching (FLIP) experiments were collected using a point scanning confocal microscope (Zeiss 780; Carl Zeiss) with a GaAsP high QE 32 channel spectral array detector with a 63x/1.4 oil Plan-Apochromat objective (Carl Zeiss) controlled by Zen software (version 2010; Carl Zeiss). Synchronized L3 hermaphrodites were anesthetized and prepared for imaging as described for time-lapse acquisition above. The FLIP region of interest (ROI) was a 25-pixel (approximately 1 μm) diameter circle placed on the perimeter of the AC along either the apical membrane of invasive protrusion membrane. Four cycles of z-stack images were acquired at 18 second intervals at with 1.0 μm slice thickness for 14 slices centered on the AC. Each cycle of acquisition was followed by a cycle of photobleaching of the FLIP ROI. Bleaching was performed at 100% laser power with 25 iterations.

All quantifications for FLIP experiments were performed in Fiji. Relative GFP loss was calculated by subtracting the pixel values of a sum projection of the AC taken at the fourth acquisition cycle (three cycles of bleaching performed every 18 seconds, then a fourth acquisition performed 54 seconds from acquisition start) from the corresponding pixel values of a sum AC projection taken at the first acquisition cycle (before any photobleaching). The resulting difference was then divided by the initial pixel intensity from the first acquisition cycle to generate a relative rate of loss. Regions for FLIP ratios were established by drawing a 3-pixel wide line across the AC to separate the two halves (for P6.p 2-cell and 8-cell controls) or by drawing a 3-pixel wide line across the AC at the neck of the invasive protrusion. The average rate of loss of the two AC regions was calculated from the relative rates of loss of the pixels in each region. FLIP ratios display the quotient of the average of the region with the photobleaching ROI (Region X) divided by the average of the region without the photobleaching ROI (Region Y). Spectral images for display purposes were generated by adding a background value of 100 to each pixel of the first acquisition cycle to eliminate background noise before the calculation of relative loss and applying the Fire lookup table in Fiji with constrained pixel ranges from 0.00 to 0.50. The resulting image was then smoothed for display. An ImageJ macro that automates this process follows (this can be downloaded at <https://sites.duke.edu/sherwoodlab/protocols/>): is available upon request.

Anchor Cell FLIP Analysis Macro

```

1. * FLIP Analysis and Heatmap Generator
2. * ImageJ/Fiji code written by Kaleb M. Naegeli, Duke University
3. * IMPORTANT: this code generates comparisons of cell regions and makes heatmaps for these
4. * regions
5. * for 1 cycle and 3 cycles of photobleaching. 3-cycle data were used in this publication.
6. * IMPORTANT: This code only works for .lsm files from a Zeiss imaging system. Image files
7. * from other systems require a code change in line 11. */
8. * IMPORTANT: you must rename/specify your own file paths in
9. * lines 19, 38, 48, 54, 64, 71, 81, and 87
10. image=getTitle;
11. //print(image);
12. tiff_name=replace(image, ".lsm", "");
13. //this makes the files that are used for later comparisons
14. run("Z Project...", "projection=[Sum Slices] all");
15. run("Slice Keeper", "first=1 last=4 increment=1");
16. run("Subtract Background...", "rolling=50 stack");
17. run("StackReg", "transformation=[Rigid Body]");
18. saveAs("Tiff", "C:\\Users\\Kaleb\\Documents\\0 Sherwood Lab\\FLIP\\780 Upright\\Macro Heatmaps\\"+tiff_name+"-pro-
    jection");
19. rename("Sum.lsm");
20. //run("Brightness/Contrast...");
21. resetMinAndMax();
22. selectWindow("Sum.lsm");

```

```

23. run("Duplicate...", "title=1.lsm duplicate range=1-1");
24. selectWindow("Sum.lsm");
25. run("Duplicate...", "title=2.lsm duplicate range=2-2");
26. selectWindow("Sum.lsm");
27. run("Duplicate...", "title=4.lsm duplicate range=4-4");
28. //cycle 1 comparisons
29. imageCalculator("Subtract create 32-bit", "1.lsm", "2.lsm");
30. rename("1sub.lsm");
31. imageCalculator("Divide create 32-bit", "1sub.lsm", "1.lsm");
32. //run("Brightness/Contrast...");
33. setMinAndMax(0.000000000, 0.500000000);
34. rename("1 cycle.lsm");
35. run("Fire");
36. saveAs("Tiff", "C:\\Users\\Kaleb\\Documents\\0 Sherwood Lab\\FLIP\\780 Upright\\Macro Heatmaps\\"+tiff_name+"-1wbg");
37. run("Duplicate...", "title=1cyctemp.tif");
38. //cycle1 mask
39. selectWindow("1.lsm");
40. run("Duplicate...", "title=1-1.lsm");
41. //run("Threshold...");
42. setAutoThreshold("Default dark");
43. run("Make Binary");
44. run("Fill Holes");
45. saveAs("Tiff", "C:\\Users\\Kaleb\\Documents\\0 Sherwood Lab\\FLIP\\780 Upright\\Macro Heatmaps\\"+tiff_name+"-MASK");
46. rename("1-1.lsm");
47. imageCalculator("AND create", "1-1.lsm", "1cyctemp.tif");
48. rename("1 cycle masked.lsm");
49. run("Fire");
50. saveAs("Tiff", "C:\\Users\\Kaleb\\Documents\\0 Sherwood Lab\\FLIP\\780 Upright\\Macro Heatmaps\\"+tiff_name+"-1mask");
51. //3 cycle comparison
52. imageCalculator("Subtract create 32-bit", "1.lsm", "4.lsm");
53. rename("3sub.lsm");
54. imageCalculator("Divide create 32-bit", "3sub.lsm", "1.lsm");
55. //run("Brightness/Contrast...");
56. setMinAndMax(0.000000000, 0.500000000);
57. rename("3 cycle.lsm");
58. run("Fire");
59. saveAs("Tiff", "C:\\Users\\Kaleb\\Documents\\0 Sherwood Lab\\FLIP\\780 Upright\\Macro Heatmaps\\"+tiff_name+"-3wbg");
60. run("Duplicate...", "title=3cyctemp.tif");
61. //3 cycle mask
62. imageCalculator("AND create", "1-1.lsm", "3cyctemp.tif");
63. rename("3 cycle masked.lsm");
64. run("Fire");
65. saveAs("Tiff", "C:\\Users\\Kaleb\\Documents\\0 Sherwood Lab\\FLIP\\780 Upright\\Macro Heatmaps\\"+tiff_name+"-3mask");
66. //smoothed comparisons images
67. selectWindow("1.lsm");
68. run("Duplicate...", "title=1add.lsm");
69. run("Add...", "value=100");
70. imageCalculator("Divide create 32-bit", "1sub.lsm", "1add.lsm");
71. setMinAndMax(0.000000000, 0.500000000);
72. run("Fire");
73. run("Smooth");
74. saveAs("Tiff", "C:\\Users\\Kaleb\\Documents\\0 Sherwood Lab\\FLIP\\780 Upright\\Macro Heatmaps\\"+tiff_name+"-1smooth");
75. imageCalculator("Divide create 32-bit", "3sub.lsm", "1add.lsm");

```

```

76. setMinAndMax(0.00000000, 0.50000000);
77. run("Fire");
78. run("Smooth");
79. saveAs("Tiff", "C:\\Users\\Kaleb\\Documents\\0 Sherwood Lab\\FLIP\\780 Upright\\Macro Heatmaps\\"+tiff_name+"-
  3smooth");
80. run("Close All");

```

Calculation of Basement Membrane Hole Opening Rates

Rates of BM hole expansion were quantified as published previously by our laboratory (Kelley et al., 2017). Time-lapse image series of AC protrusion formation acquired as described above were reconstructed in 3D using Imaris 7.6.5 (Bitplane, Inc.) The 3D-rendered BM was rotated 90° about the anterior-posterior axis of the worm to view the ventral surface of the animal. The signal from the BM fluorescence channel only was then exported as a TIFF series. This series was opened in Fiji and BM hole size was then analyzed at five minute intervals through the time-lapse series by manually thresholding the BM hole and measuring the area of the thresholded region.

Blinding and Unbiasing of Data

For polarity and fluorophore intensity measurements, data sets were randomized using an ImageJ macro (courtesy of Martin Hoehne) to blind analysis. For samples in which blind analysis was not possible, randomly-selected samples were chosen for re-analysis to confirm precision of measurements.

Statistical Analysis and Data Presentation

Statistical analyses were performed using JMP version 12.0 (SAS Institute). For all figure legends, asterisks indicate statistical significance as follows: n.s. = not significant ($p > 0.05$); * $p < 0.05$; ** $p < 0.01$; *** $p < 0.001$. All comparisons of means were accomplished using a two-tailed unpaired Student's t test or One-way ANOVA with Tukey HSD post-hoc test as appropriate, and the specific test used and all sample sizes are indicated in the corresponding figure legend. For comparisons of parametric samples in which statistically significant differences were observed, sample sizes and distributions were validated by assaying normality of variance using a Shapiro-Wilk's normality test. All data sets displayed normal variance with the exception of protrusion size in the wild type animals shown in Figure S1G (Figure S1G). Figures and graphs were constructed using Excel 2010 (Microsoft) and Illustrator (CC 2015; Adobe).